

Quarterly Report for
Contract DE-FG36-02ID14418
Stanford Geothermal Program
October-December 2004

Table of Contents

1. THEORETICAL STUDY OF PHASE TRANSFORMATION EFFECTS ON STEAM-WATER RELATIVE PERMEABILITIES	1
1.1 INTRODUCTION	1
1.2 INVISCID BUBBLE TRAIN MODEL	2
1.3 DISCUSSION	11
1.4 CONCLUSION	16
2. INFERRING RELATIVE PERMEABILITY FROM RESISTIVITY WELL LOGGING	19
2.1 SUMMARY	19
2.2 INTRODUCTION	19
2.3 MATHEMATICAL MODELS	19
2.4 RESULTS	21
2.5 CONCLUSION	28
3. FRACTURED ROCK RELATIVE PERMEABILITY	29
3.1 BACKGROUND	29
3.2 EXPERIMENTAL METHODOLOGY	31
3.3 THEORETICAL BACKGROUND FOR ELECTRICAL RESISTIVITY	31
3.4 NITROGEN-WATER RELATIVE PERMEABILITY EXPERIMENTAL METHOD	32
3.5 NITROGEN-WATER RELATIVE PERMEABILITY RESULTS IN BEREA SANDSTONE	33
3.6 RESULTS OF ELECTRICAL RESISTIVITY IN RELATIVE PERMEABILITY MEASUREMENTS	34
3.7 ELECTRICAL RESISTIVITY RESULTS IN GEOTHERMAL ROCK	35
3.8 CONTINUING AND FUTURE WORK	38
4. ELECTRICAL IMPEDANCE TOMOGRAPHY (EIT) METHOD FOR SATURATION DETERMINATION	39
4.1 INTRODUCTION	39
4.2 THE EIT APPARATUS	41

4.3 CONTINUING AND FUTURE WORK	42
5. MEASUREMENTS OF IN-SITU WATER SATURATION IN DIFFERENT GEOTHERMAL ROCKS	43
5.1 SUMMARY	43
5.2 CURRENT STATUS	45
5.3 CONCLUSIONS	45
6. DOWNHOLE ENTHALPY MEASUREMENT	47
6.1 SUMMARY	47
6.2 ENTHALPY MEASUREMENTS	47
6.3 WHY MEASURE ENTHALPY?	49
6.4 PROPOSED METHODS AND PRESENT STATUS	49
6.5 CONCLUSION	52
7. REFERENCES	53

1. THEORETICAL STUDY OF PHASE TRANSFORMATION EFFECTS ON STEAM-WATER RELATIVE PERMEABILITIES

This project is being conducted by Research Assistant Chih-Ying Chen and Prof. Roland Horne. The goal of this research is to model the effects of phase transformation on steam-water relative permeabilities and explain the behavior of enhanced steam-phase relative permeabilities (presented previously) obtained from experiments of steam-water in fractures. In this study, the inviscid bubble train model based on the Bretherton theory was used and coupled with the relative permeability concepts. The phase transformation effects were evaluated by introducing the interfacial mass flux based on the carry-away and precipitation processes of vapor molecules. Results from this model are qualitatively in accordance with our earlier experimental measurements. Besides the quantitative investigation, idealized toroidal throat geometry was used to illustrate the efficient transport that occurs in the steam (vapor) phase. The more efficient substitution transport may occur when steam bubbles are transported through the pore throats. This may be another characteristic contributing to the enhancement of steam-phase relative permeabilities.

1.1 INTRODUCTION

Boiling phenomena occur in geothermal reservoirs when the reservoir pressure is less than the saturated pressure at the reservoir temperature. Boiling generates unconventional two-phase flow because of phase transformations, which affect multiphase flow in geothermal reservoirs due to the same substance occurring in different phases. Phase transformation effects also change the phase behavior and the flow characteristics (Chen et al., 2004).

In geothermal reservoir simulations, it has long been debated whether these effects influence the relative permeability functions significantly (Verma, 1986; Horne et al., 2000; Chen et al., 2004; Schechter and Schechter, 1987; Piquemal, 1994). Several studies suggested that in porous media, the steam-water relative permeability curves behave similarly to the air-water relative permeability curves (Schechter and Schechter, 1987; Piquemal, 1994). However, another set of studies suggested that steam-water relative permeability curves in porous media behave differently from air-water curves (Verma, 1986; Satik, 1998; Horne et al., 2000; Chen et al., 2004). These studies showed that the steam-phase relative permeability is enhanced in comparison to the air-phase relative permeability. Among these studies, none were conducted theoretically considering the saturated, superheated and subcooling thermodynamics as well as interfacial mass flux, except for the study done by Verma (1986), where he conducted theoretical and numerical studies of the phase transformation effects on steam-water flow in porous media. In an idealized toroidal geometry, Verma (1986) concluded that the phase transformation phenomenon results in a lower pressure drop across the flow channel and can lead to enhancement of steam phase relative permeabilities in high conductivity media. However, the direct theoretical or numerical investigation of how the phase transformation effects influence relative permeabilities was not conducted.

One uncomplicated method to study the steam-liquid transport theoretically is to consider it as the motion and interactions of discrete bubble trains (or droplet trains) in capillary

tubes. These bubble train models were generally used to study pore network models for gas-water or foam-water flow behaviors (Foulser et al., 1991; Babchin and Yuan, 1997; Stark and Manga, 2000). Hunt and Manga (2003) studied the effects of noncondensable gas bubbles on the hydraulic conductivity using Bretherton's theory and suggested a capillary-number-dependant liquid relative permeability function. However, the gas (bubble) relative permeability function was absent. Furthermore, none of these earlier studies have conducted an evaluation of the effects of phase transformation on the steam bubbles flow in this simple geometry.

This study may be deemed a preliminary evaluation of the effects of phase transformation on steam-water (vapor-water) flow behavior in terms of the relative permeability concept by using the theory of the moving of bubble trains in cylindrical capillary tubes. Several complicated interfacial physical chemistry and thin film effects were ignored at this stage. This study was organized as follows: we first derived conventional, noncondensable gas-water relative permeability. Steam-water relative permeability functions with phase transformations were then introduced by using the kinetic theory of gas. After that, a torroidal pore throat was used to demonstrate qualitatively the transport differences between steam-water flow and noncondensable gas-water flow. Finally, we outlined the preliminary conclusions in preparation for future work. To avoid confusion, terms of “*air*” or “*noncondensable gas*” are used to refer to the gas phase in multiphase flow without phase transformations, while terms of “*steam*” or “*vapor*” are used to refer to the gas phase in multiphase flow with phase transformations.

1.2 INVISCID BUBBLE TRAIN MODEL

1.2.1 Model Description

The inviscid bubble train model considers the gas phase inside the bubble as an inviscid fluid which does not obey a linear pressure-velocity relation. This is generally referred to as Bretherton bubble behavior (Bretherton, 1961). When an inviscid long bubble is inserted into the cylindrical capillary in which a Newtonian liquid is flowing, the pressure-velocity relation becomes nonlinear due to several mechanisms active around the bubble, which include the drag of the bubble, the film lubrication as well as the pushing force done by the liquid (Wong et al., 1995a, 1995b; Ratulowski and Chang, 1989). Hunt and Manga (2003) studied the effects of bubbles on the hydraulic conductivity using Bretherton's theory and suggested a capillary-number-dependant liquid relative permeability function. However, the gas relative permeability was claimed to be meaningless and thus was absent in their study, as the gas phase is not continuous.

Though the gas phase is discontinuous at the instantaneous scale, it may be considered as continuous on average at the macroscopic scale if the gas phase is in a form of a homogeneous bubble train. To embed relative permeability concepts and couple phase transformation effects in these models, the consideration of gas viscosity and interfacial mass flux due to phase transitions becomes critical. In this section, we first modify the theoretical derivation from the study of Hunt and Manga (2003) and then study the phase

transformation effects on the relative permeability functions obtained by introducing the concept of the interfacial mass flux in a steam-water system.

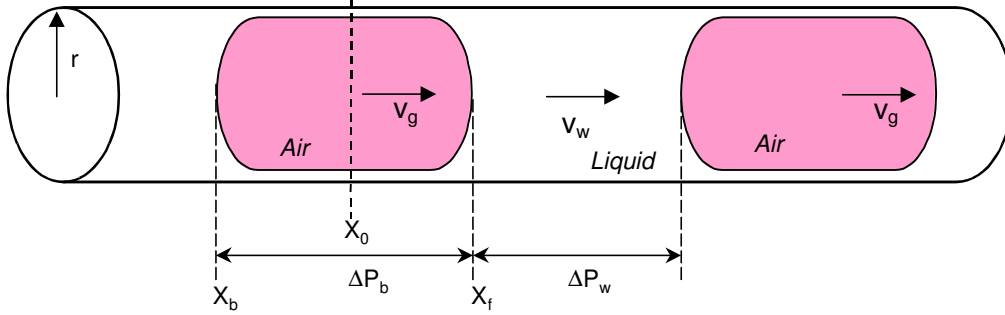


Figure 1.1: Schematic of motion of a homogeneous bubble train containing long air bubbles in a cylindrical capillary tube.

Considering the motion of long bubbles in Figure 1.1, for small Reynolds number, Bretherton (1961) used a matched-asymptotics method in deriving the motion of long bubbles in a circular capillary. The relationship between average bubble velocity and liquid velocity is suggested as:

$$v_g = \frac{v_w}{1 - \omega} \quad (1.1)$$

where v_g and v_w are bubble and liquid velocities respectively, and:

$$\omega = 1.29(3Ca)^{2/3} \quad \text{and} \quad Ca = \frac{\mu_w v_g}{\sigma} \quad (1.2)$$

where σ is the interfacial tension, Ca is the capillary number, and μ_w is the water dynamic viscosity.

As shown in Equation (1.1), the relationship between the average bubble velocity and liquid velocity is nonlinear, and the average bubble velocity exceeds the average liquid velocity by a factor of ω . For small Reynolds number and slow moving fluids, the coefficient ω is very small for noncondensable gas bubbles. Bretherton's study showed that the pressure drop across a bubble (ΔP_b) and the liquid film between the bubble and tube wall (h_∞) also scales as $Ca^{2/3}$ for a sufficient small Ca . This pressure drop can be expressed as:

$$\Delta p_b = 3.58 \frac{\sigma}{r} (3Ca)^{2/3} \quad (1.3)$$

where r is the radius of the capillary tube.

The total pressure drop across the tube and the length of the tube are:

$$\Delta p_t = \sum \Delta p_w + \sum \Delta p_b \quad (1.4)$$

$$L_t = \sum L_w + \sum L_b \quad (1.5)$$

The saturation is defined as the length ratios:

$$S_w = \frac{\sum L_w}{L_t} \quad \text{and} \quad S_g = \frac{\sum L_b}{L_t} \quad (1.6)$$

For a long bubble train shown in Figure 1.1, every bubble has an identical volume, V_b ; therefore, the total volume of gas (vapor) in the bubble train can be expressed as:

$$N_b V_b = \pi r^2 \sum L_b = \pi r^2 L_t S_g \quad (1.7)$$

and the number of bubbles can be written as:

$$N_b = \frac{\pi r^2 L_t S_g}{V_b} \quad (1.8)$$

where N_b is the number of bubbles in the bubble train.

The total pressure drop of bubbles throughout the tube is then:

$$\sum \Delta p_b = N_b \frac{3.58\sigma}{r} (3Ca)^{2/3} \quad (1.9)$$

Applying the relationship in Equation (1.1), Equation (1.9) can be rewritten as:

$$\sum \Delta p_b = N_b \frac{7.45 \left(\frac{\sigma}{r}\right) \left(\frac{\mu_w q_w}{\sigma \pi r^2}\right)^{2/3}}{(1-\omega)^{2/3}} \quad (1.10)$$

Since the liquid phase is continuous Newtonian fluid, the Poiseuille equation can be used to calculate the total liquid pressure drop. For a steady-state, continuous flow, the water rate can be expressed as:

$$q_{w,p} = \frac{\pi r^4}{8\mu_w} \frac{\Sigma \Delta p_w}{\Sigma L_w} \quad (1.11)$$

As one can imagine, the flow of bubble train is in quasisteady state (or pulsed steady state) in the instantaneous sense. There are alternative single-phase instantaneous flows passing through a specific cross section. To apply two-phase generalized Darcy's equation and account for the alternative flow, the void (gas) portion has to be excluded from the flowing water phase. Therefore, the average water flow rate was obtained by multiplying Equation (1.11) by water saturation:

$$q_{w,avg} = S_w q_{w,p} \quad (1.12)$$

From Equations (1.11) and (1.12), the total liquid pressure drop is:

$$\Sigma \Delta p_w = \frac{8\mu_w \Sigma L_w}{\pi r^4} q_{w,p} = \frac{8\mu_w \Sigma L_w}{S_w \pi r^4} q_w \quad (1.13)$$

To impose the relative permeability concept into this model, the total pressure drop throughout the capillary has to be related to the generalized Darcy equation. Considering the water phase, according to Darcy's law, the water flow rate is defined as:

$$q_w = \frac{kk_{rw} A}{\mu_w} \frac{\Delta p_t}{L_t} \quad (1.14)$$

For a cylindrical tube:

$$k = \frac{r^2}{8} \quad \text{and} \quad A = \pi r^2 \quad (1.15)$$

The bubble and the liquid velocities is related to the Darcy velocities by:

$$v_w = \frac{u_w}{S_w} = \frac{kk_{rw}}{S_w \mu_w} \frac{\Delta p_t}{L_t} \quad (1.16)$$

$$v_g = \frac{u_g}{S_g} = \frac{kk_{rg}}{S_g \mu_g} \frac{\Delta p_t}{L_t} \quad (1.17)$$

Thus:

$$\frac{v_w}{v_g} = \frac{S_g k_{rw} \mu_g}{S_w k_{rg} \mu_w} \quad (1.18)$$

From Equations (1.14) and (1.15) the total pressure drop can be expressed as:

$$\Delta p_t = \frac{8\mu_w L_t}{\pi r^4 k_{rw}} q_w \quad (1.19)$$

Substituting Equations (1.10), (1.13) and (1.19) into Equation (1.4), yields:

$$\frac{8\mu_w L_t}{\pi r^4 k_{rw}} q_w = \frac{8\mu_w \sum L_w}{S_w \pi r^4} q_w + N_b \frac{7.45 \left(\frac{\sigma}{r}\right) \left(\frac{\mu_w q_w}{\sigma \pi r^2}\right)^{2/3}}{(1-\omega)^{2/3}} \quad (1.20)$$

Reducing and solving Equation (1.20) for k_{rw} , we obtain:

$$k_{rw} = \frac{1}{1 + 0.931 \frac{\pi r^3 (1-S_w)}{V_b} \frac{Ca^{-1/3}}{(1-\omega)^{2/3}}} \quad (1.21)$$

To evaluate the gas-phase relative permeability function and impose the generalized Darcy equations, the gas viscosity still has to be applied even though the gas phase is considered inviscid for Bretherton's derivations. As the relationship between average bubble velocity and liquid velocity is nonlinear, we used the velocity ratio method to evaluate the gas-phase relative permeabilities with and without the effects of phase transformation. For the gas-water flow without phase transformation effects, combining Equations (1.18) and (1.1), we obtain:

$$\frac{v_w}{v_g} = \frac{S_g k_{rw} \mu_g}{S_w k_{rg} \mu_w} = 1 - \omega \quad (1.22)$$

Therefore:

$$k_{rg} = \frac{(1-S_w) \mu_g}{S_w \mu_w (1-\omega)} k_{rw} \quad (1.23)$$

Substituting Equation (1.21) into Equation (1.23), the noncondensable gas relative permeability is then:

$$k_{rg} = \frac{\left[\frac{(1-S_w)\mu_g}{S_w\mu_w(1-\omega)} \right]}{\left[1 + 0.931 \frac{\pi r^3 (1-S_w) Ca^{-1/3}}{V_b (1-\omega)^{2/3}} \right]} \quad (1.24)$$

Equations (1.21) and (1.24) are used as the base relative permeability functions for conventional gas-water flow without phase transformations.

1.2.2 Interfacial Flux for Vapor Bubbles in a Capillary

For vapor-liquid flow in a cylindrical tube in isothermal equilibrium, the phase transformations enhance the flow of vapor bubbles due to vaporization-condensation effects. Here, flow of a vapor bubble train in a capillary tube is used to evaluate the interfacial mass flux and the movement of interface. The bubble train is assumed homogeneous with identical bubbles and spacing. As shown in Figure 1.2, due to the pressure drop across the bubble, vaporization occurs at the leading interface of the bubble, while condensation occurs on the trailing interface of the bubble as the system is at isothermal conditions. This vaporization-condensation phenomenon not only makes the liquid molecular transport through the vapor bubble via vaporization-then-condensation, but also enhances the bubble velocity because of the extra displacement of the bubble contributed by the vaporization-condensation effects. To quantify the magnitude of these effects, the following assumptions were adopted in this model:

- 1) System is in isothermal condition; $T(\text{liquid}) = T(\text{vapor}) = T(\text{tube wall}) = \text{constant}$.
- 2) $p_v = p_{sat}(T_v) = \text{constant}$. Flat interface occurs at $x = x_0$; therefore, $P_v = P_l(x=x_0)$.
- 3) The bubble is long enough that the curvature of the front and end caps of the bubble can be ignored for the interfacial mass flux calculation. In other words, the bubble is considered as cylindrical shape in calculating the interfacial mass flux.
- 4) The thin film between the bubble and the tube wall is small and the phase transformations within it are small and do not affect the longitudinal interfacial mass flux in the previous assumption.

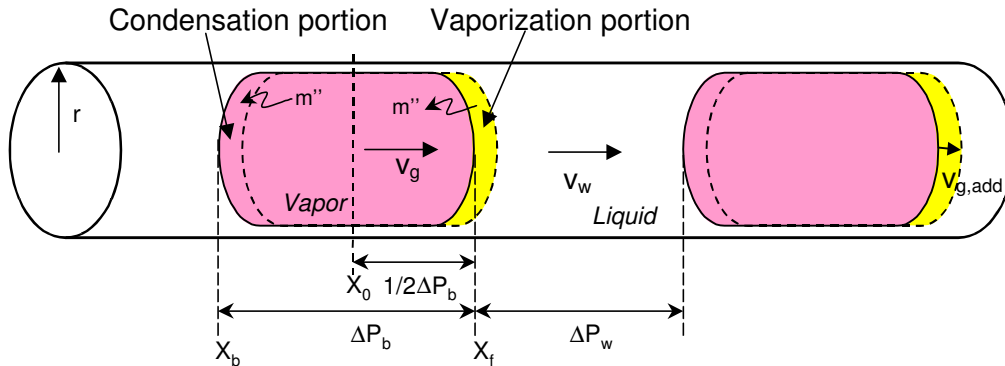


Figure 1.2: Schematic of motion of a homogeneous bubble train containing long vapor bubbles in a cylindrical capillary tube.

Considering a single saturated vapor bubble surrounded by moving liquid, x_0 is the center position of the bubble, x_f and x_b are the front and back ends of the bubble, and m'' is the interfacial mass flux due to vaporization or condensation. Due to the pressure difference (Δp_b) across the bubble, vaporization takes place in the front cap and causes the inward mass flux, while condensation takes place in the back cap and causes the outward mass flux as shown in Figure 1.2. Under equilibrium, these two interfacial mass flux are equal but in different sign resulting in an extra average velocity ($v_{g,add}$) of the bubble besides the original average velocity in Equation (1.1). The interfacial mass flux was calculated from the kinetic theory of vapor molecules (Silver and Simpson, 1961):

$$m'' = \left[\frac{2\hat{\sigma}}{(2 - \hat{\sigma})} \right] \left(\frac{\bar{M}}{2\pi\bar{R}} \right)^{1/2} \left(\frac{P_v}{T_v^{1/2}} - \frac{P_l}{T_l^{1/2}} \right) \quad (1.25)$$

where $\hat{\sigma}$ is the accommodation coefficient ($\hat{\sigma}=0.4$ is employed (Fujikawa and Maerefat, 1990)) and \bar{M} is the molecular weight. \bar{R} is the gas constant. This equation has also been referred to as the Hertz-Knudsen-Langmuir formula or Kucherov-Rikenglaz equation in the Soviet literature (Carey, 1992; Kucherov and Rikenglaz, 1960; Akhatov et al., 2001).

Considering the assumptions listed above and the leading (right) cap of the bubble where the vaporization prevailing, the pressure difference between the liquid phase and vapor phase can be expressed as:

$$P_v - P_l = P_l(x=0) - P_l(x=x_f) = \frac{1}{2} \Delta P_b \quad (1.26)$$

The mass flux passing through the leading interface (at $x=x_f$) becomes:

$$m'' = \left[\frac{2\hat{\sigma}}{(2 - \hat{\sigma})} \right] \left(\frac{\bar{M}}{2\pi\bar{R}} \right)^{1/2} \left(\frac{0.5\Delta p_b}{T^{1/2}} \right) \quad (1.27)$$

The extra velocity due to phase transformation effects is then obtained by dividing Equation (1.27) by the liquid density:

$$v_{g,add} = \left[\frac{2\hat{\sigma}}{(2 - \hat{\sigma})} \right] \left(\frac{\bar{M}}{2\pi\bar{R}} \right)^{1/2} \left(\frac{0.5\Delta p_b}{\rho_w T^{1/2}} \right) \quad (1.28)$$

To incorporate the extra bubble velocity in Equation (1.28) and evaluate the effects of phase transformation on liquid-vapor relative permeabilities, we may introduce:

$$\varepsilon = \frac{v_w}{v_g + v_{g,add}} = \frac{S_g k_{rw} \mu_g}{S_w k_{rg} \mu_w} \quad (1.29)$$

where $v_{g,add}$ is obtained from Equation (1.28) in which Δp_b is calculated from Equation (1.3). The liquid-phase relative permeability remains unchanged, as the net mass flux due to vaporization and condensation does not affect the net movement of the liquid phase. By using the velocity ratio method illustrated previously, the enhanced vapor-phase relative permeability is then given by:

$$k_{rg} = \frac{\left[\frac{(1 - S_w) \mu_g}{S_w \mu_w \varepsilon} \right]}{\left[1 + 0.931 \frac{\pi r^3 (1 - S_w) Ca^{-1/3}}{V_b (1 - \omega)^{2/3}} \right]} \quad (1.30)$$

1.2.3 Modeling Results

In this section, we compare the relative permeabilities with and without phase transformation effects using the inviscid bubble train model. As can be seen in Equations (1.21) and (1.24), the relative permeability functions are not unique and hence depend on the capillary number. To evaluate these functions, we first solved the nonlinear bubble velocity according to the specified liquid velocity and then calculated ω and Ca and Δp_b . Unlike in a Newtonian fluid, the Δp_b does not depend on the bubble length, but depends on the Ca , σ and r as shown in Equation (1.3). To calculate the enhancement of the steam relative permeabilities, the capillary radius (r) was adjusted to generate different values of Δp_b . The parameters used for calculating the steam-water relative permeabilities are illustrated in Table 1.1.

Table 1.1: Fluid properties and parameters used in the inviscid bubble train model.

Temperature; T (°C)	104
Water density; ρ_w (kg/m ³)	955.44
Water viscosity μ_w (cp)	0.2703
Steam viscosity μ_g (cp)	0.0124
Interfacial tension; σ (N/m)	0.0580
Accommodation coef.; $\hat{\sigma}$	0.4
Molecular weight. \bar{M} (kg/kmole)	18
Gas constant; \bar{R} (J/kmole-K)	8314.4
Single bubble volume; V_b	$1.5 \times \left(\frac{4}{3} \pi r^3 \right)$
Water velocity; v_w (m/s)	0.01

By using Equation (1.21) and Table 1.1, the water-phase relative permeabilities, k_{rw} , is shown in Figure 1.3 for different capillary number, Ca^* defined as

$$Ca^* = \frac{\mu_w v_w}{\sigma} \quad (1.31)$$

For slow and constant average water velocity, most of the k_{rw} curve follows the typical behavior. However, k_{rw} cannot approach zero as it moves close to the end point ($S_w=0$), which shows an unphysical asymptotic. In addition, relative permeabilities increase with the increase of Ca^* ; however the unphysical artifact also increases. This can be attributed to the neglecting of the steam viscosity, challenges of the slow moving assumptions as well as some hypothesis in calculating Δp_b . Moreover, Bretherton's theory is suggested at low Reynolds number, low capillary number and for long bubbles (Bretherton, 1961; Olbricht, 1996) and it performs poorly as these restrictions becomes weaker. This may demonstrate the inconsistency and incompatibility of applying the “inviscid” Bretherton theory to the “viscous-dominant” generalized Darcy equations, because this inviscid model is controlled by the capillary number referenced to the average fluid velocity and the single bubble volume (or length).

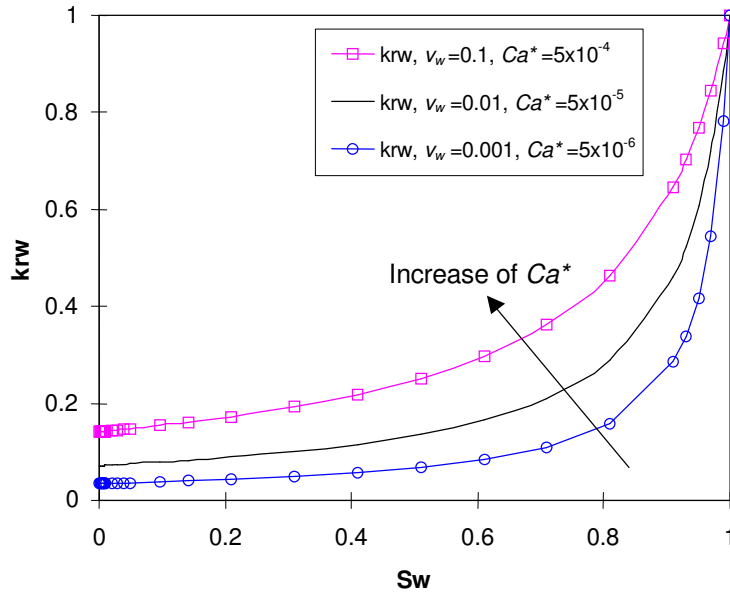


Figure 1.3: Water-phase relative permeability as function of capillary number, Ca^* , in inviscid bubble train model.

Despite this fact, we can still evaluate the effects of the phase transformation qualitatively if the Ca^* is kept small. By using Equations (1.21), (1.24) and (1.30), Figure 1.4 shows steam-water relative permeabilities of the inviscid bubble train model with and without phase transformation effects. The bubble pressure drop was adjusted to 1, 2 and 10 psig in evaluating the phase transformation effects. Figure 1.4a shows the linear plot of relative permeability curves in this inviscid model and Figure 1.4b is the logarithmic plot of them.

The enhancement of the steam-phase relative permeabilities due to phase transformation effects are less evident in the linear plot because the values of the based k_{rg} are very small over most of the S_w range. However the logarithmic plot in Figure 1.4b more clearly shows the enhancement of the steam phase mobility in the three cases. In the aspect of the phase transformation effects, the larger the bubble pressure drop, the more enhanced the steam relative permeabilities behave. However, the magnitude of the enhancement in this model is not very significant because of the extremely small values in most of the based k_{rg} curve.

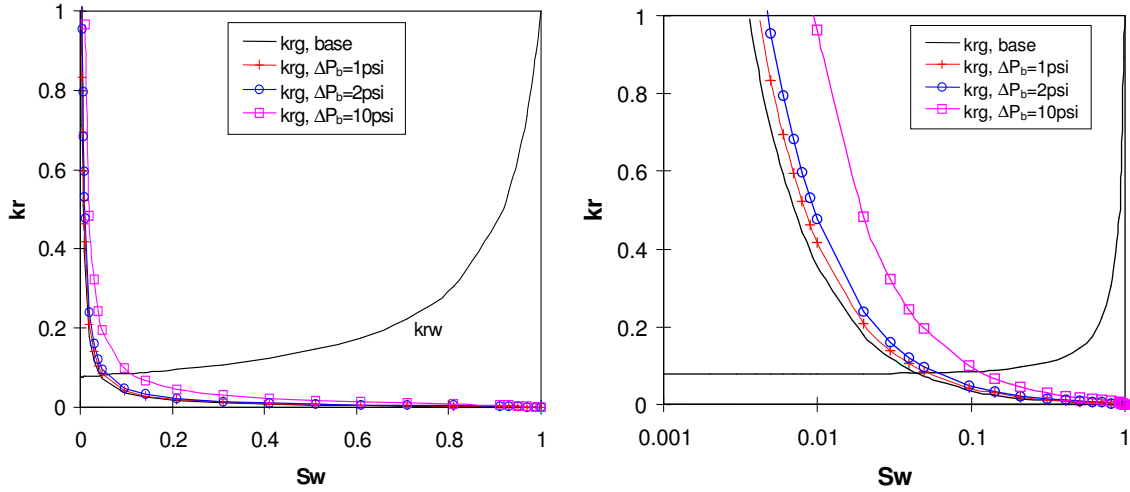


Figure 1.4: Steam-water relative permeabilities of the inviscid bubble train model: (a) linear plot, (b) logarithmic plot. ($Ca^* = 10 \times 10^{-5}$)

1.3 DISCUSSION

In this study we have suggested a simplified model to evaluate the effects of the phase transformation on steam-water relative permeabilities. The interfacial mass flux in steam-water saturated or close-to-saturated condition is a difficult issue which has not been fully understood, because it involves saturated thermodynamics, unstable phase behaviors, thermal-capillary behaviors and other physical chemistry problems. The interfacial mass flux equation based on the kinetic theory of gas was employed in this study. Comparing these theoretical results to the measurements shown in Figure 1.5, the theoretical results show qualitative consistency with our measurements of steam-water relative permeabilities. The shapes of curves from theory and measurement show significant discrepancy, as is to be expected. Hence, quantitative interpretations using suggested models are not suggested currently for several reasons. First of all, the cylindrical capillary is inherently different geometrically from the fractures used in the experiments. Regarding the corresponding flow structures, as discussed in previous quarterly reports, the observed flow structures of steam-water flow in the fractures are complex combinations of bubbles, slugs and unstable channels. These complex structures certainly generate different curves of relative permeability from those considering only bubble flow. Moreover, the ignored capillary pressure and gravity (buoyancy) effects as well as the assumptions used in the

models may be important factors in the situation of the smooth-fracture and rough-fracture experiments.

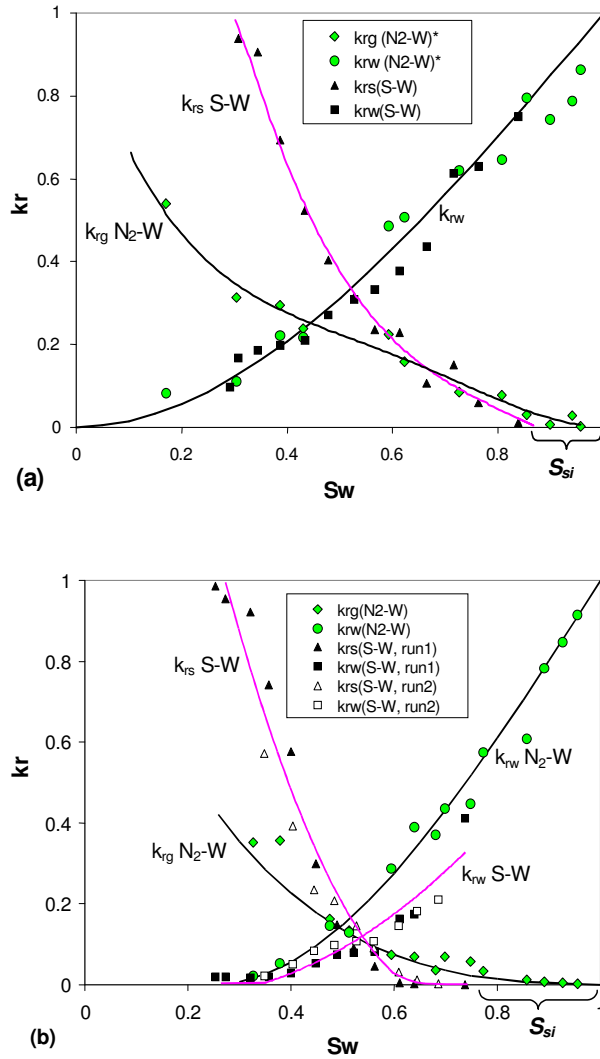


Figure 1.5: From Chen et al. 2004. Average steam-water and air-water relative permeabilities measured from (a) smooth-walled fracture, (b) rough-walled fracture.

For the steam-water experiments in the rough-walled fractures, the local aperture variation may also enhance steam flow. The aperture variation is assumed to be represented by an idealized torroidal geometry as shown in Figures 1.6 and 1.7, which illustrate the intrinsic difference between steam-water transport and air-water transport through a torroidal throat. For the steam-water transport, after the bubbles contact the solid body, unlike the conventional metamorphic transport in the air-water case, the steam bubble may perform a more efficient transport behavior, called substitution transport. As shown in Figure 1.6b and 6c, after arriving at the upstream throat entry, the steam bubble first blocks the entry and causes the downstream water pressure, $p_{w,d}$, to approach zero if surface film flow is negligible. The bulk steam bubble in the upstream is condensing due to the small increase

of the upstream water pressure, $p_{w,u}$. The heat released due to condensation then transports through the contacted solid bodies via conduction. This extra energy and lower downstream pressure generate steam nucleation behavior near the downstream exit due to the change of the thermodynamic properties. As this process continues, the steam bubble condensing in the upstream entry eventually disappears, and an equal-volume steam bubble generated in the downstream exit departs. On the other hand, the major behavior occurring in the air-water transport through the throat is the bubble metamorphic transport controlled by the mechanism of capillary allowance as shown in Figure 1.7. If we define the minimum condensing pressure to initiate the condensation in the prevailing temperature as p_{cond} and the pressure drop across the throat as

$$\Delta p_{throat} = p_{w,u} - p_{w,d} \quad (1.32)$$

The maximum capillary pressure through the throat is

$$P_{C,M} = \frac{2\sigma}{r_t} \quad (1.33)$$

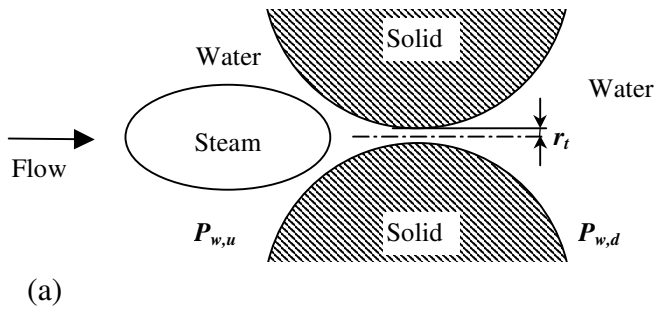
The condition needed to create the substitution transport of the steam bubble is

$$p_{w,u} > p_{cond} \quad (1.34)$$

On the other hand, the condition needed to create the metamorphic transport of the air bubble is

$$\Delta p_{throat} > P_{C,M} \quad (1.35)$$

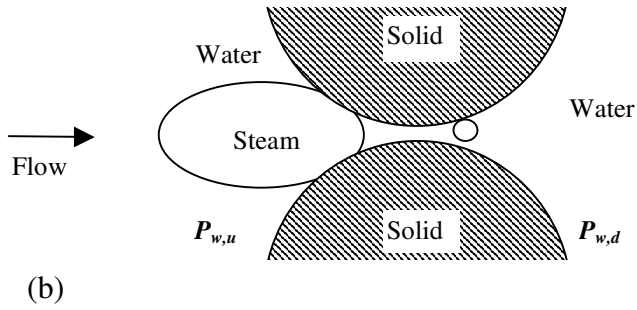
Generally speaking, Condition (1.34) is easier to reach than Condition (1.35) if the throat is small. In steam-water equilibrium conditions, only a slight increment of the pressure can condense the steam phase before the steam bubble passes through the throat, whereas the capillary pressure in air-water flow resists the air bubble in the throat may be much larger due to the small throat radius, r_t . Even though a whole fracture space constituted by lots of torroidal throats is considered, these two conditions compete for preferential transport in the steam-water flow; whereas, only Condition (1.35) can possibly occur in the air-water flow. Therefore, steam-phase transport is more efficient than the air-phase transport for similar pressure and temperature conditions, which enhances the steam phase relative permeabilities.



Arrival

$$\Delta P_{throat} = P_{w,u} - P_{w,d}$$

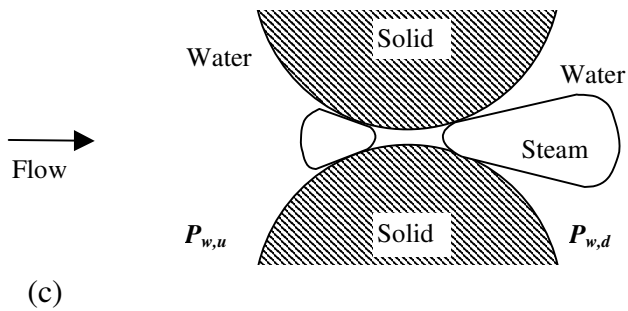
$$P_{C,M} = \frac{2\sigma}{r_t}$$



Block-Nucleation

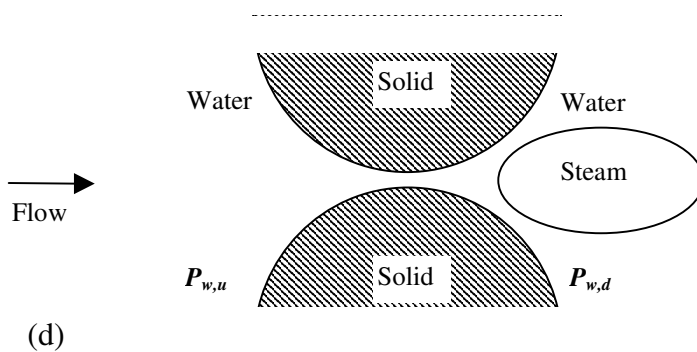
$$P_{w,u} \sim P_{cond}$$

$$P_{w,d} \sim 0$$



Substitution transport

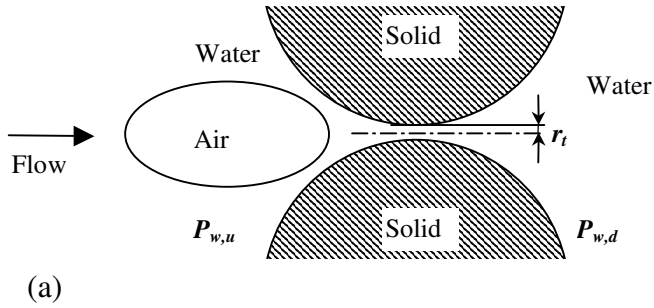
$$\Delta P_{throat} \leq P_{C,M}$$



Departure

$$\Delta P_{throat} = P_{w,u} - P_{w,d}$$

Figure 1.6: Schematic of a steam bubble transporting through an idealized torroidal geometry.

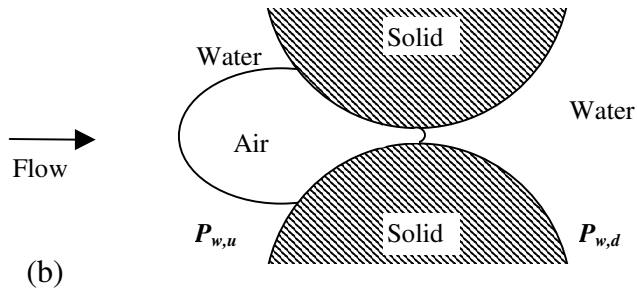


Arrival

$$\Delta P_{throat} = P_{w,u} - P_{w,d}$$

$$P_{C,M} = \frac{2\sigma}{r_t}$$

(a)

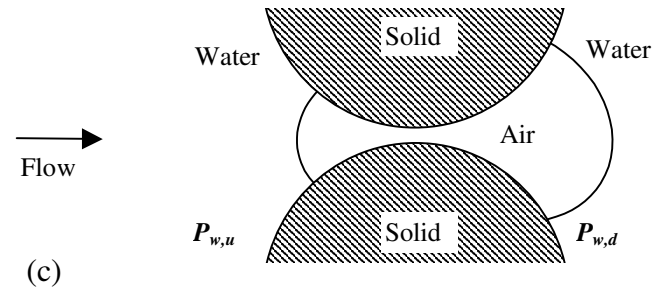


Block-squeezing

$$\Delta P_{throat} = P_{C,M}$$

$$P_{w,d} \sim 0$$

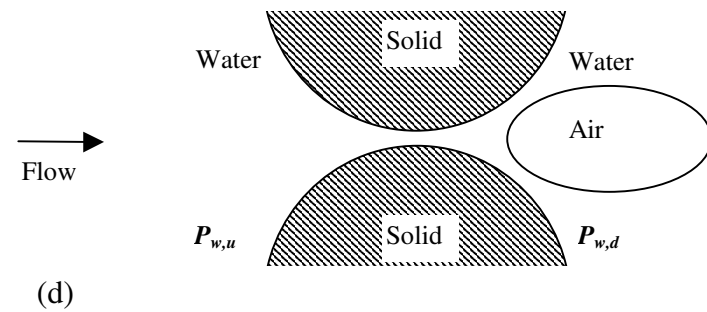
(b)



Metamorphic transport

$$\Delta P_{throat} = P_{C,M}$$

(c)



Departure

$$\Delta P_{throat} = P_{w,u} - P_{w,d}$$

(d)

Figure 1.7: Schematic of an air bubble transporting through an idealized torroidal geometry.

Verma (1986) studied the effects of phase transformation on effective permeability of channel flows of steam and water through a torroidal throat using semianalytic solution of the balance equations and entropy generation equations. The dimensionless enhancement coefficient due to phase transformations is defined as:

$$En = \frac{(T_{in} - T_{out})_0 - (T_{in} - T_{out})_{PT}}{(T_{in} - T_{out})_0} \times 100 \quad (1.36)$$

where T_{in} and T_{out} are the temperatures at the inlet face and outlet face of the torroidal throat, respectively. Subscript ($_{PT}$) denotes the solution with phase transformation, while subscript ($_0$) denotes the solution without phase transformation. Through his analytic study, Verma found that the degree of constriction of the torroidal geometry has a significant effect on effective permeability enhancement. In the aspect of the advection efficiency, Verma also concluded that the phase transformation phenomenon results in a lower pressure drop across the flow channel and can lead to enhancement of steam phase relative permeabilities in high conductivity media. Although no direct influence on relative permeabilities were discussed by Verma (1986), his results are in accordance with the observation in the current study, which is that “steam or vapor flows in a more efficient way than noncondensable gas.”

1.4 CONCLUSION

In this study, the interfacial mass flux equation based on the kinetic theory of gas was used to evaluate the effects of phase transformation on vapor bubble transport. Based on earlier studies, a bubble train model was utilized to derive the relative permeability functions accounting for the phase transformation effects. The suggested inviscid bubble train model provided a successful qualitative explanation of our experimental measurements. The shapes of the relative permeability curves from calculation and from measurements were not alike owing to the geometry and flow structure difference as well as the neglect of some physics in the simplified models.

Aside from the bubble train model, a simulated torroidal geometry model was used to demonstrate the enhanced efficiency of steam bubble transport. The thermodynamically controlled substitution transport of steam bubbles is more efficient than the conventional capillarity-controlled metamorphic transport of air bubbles. This is another factor contributing to the enhancement of steam-phase relative permeabilities.

Despite the qualitative consistency in this preliminary investigation, more rigorous assumptions and theoretical studies are needed to model and match the results obtained from the experiments. To this end, the ongoing and suggested future work are focusing or will be focused on a single-layer network model for steam transport through torroidal throats, bubble train models in fracture geometry and the pressure and temperature relationships between liquid and bubble phases.

2. INFERRING RELATIVE PERMEABILITY FROM RESISTIVITY WELL LOGGING

This research project is being conducted by Senior Research Engineer Kewen Li and Prof. Horne. The objective of this project is to develop a field method for determining relative permeability, by deriving a semianalytical model to infer relative permeability from resistivity data.

2.1 SUMMARY

Steam-water relative permeability can be calculated from capillary pressure. However this technique still requires measurement of capillary pressure. In this study, a semianalytical model was developed to infer relative permeability from resistivity data. Although it would still be necessary to conduct experimental measurements of resistivity, these are easier than measuring capillary pressure. On the other hand, resistivity data are commonly available from routine well logging. The semianalytical model was tested against experimental data. The results demonstrated that the relative permeabilities calculated from resistivity data using the new model were close to those calculated from capillary pressure data. The model developed in this study may also provide an approach to estimate permeability using both the resistivity well logging and well testing.

2.2 INTRODUCTION

One important parameter in geothermal reservoir engineering is steam-water relative permeability. Yet it is difficult to measure steam-water relative permeability because of mass transfer and phase transformation as pressure changes. Previously, Li and Horne (2002, 2004) reported that steam-water relative permeability could be calculated from capillary pressure data. These models provide an easier and more economical approach to obtain steam-water relative permeability, compared to the experimental technique. The disadvantage is the need to measure steam-water capillary pressure, which can also be difficult and time consuming in many cases. It would be helpful for engineers and scientists to have a method to infer steam-water relative permeability from resistivity data because it is easier to measure and resistivity data may be available from well logging. In this study, a semianalytical model was developed to infer relative permeability from resistivity data.

2.3 MATHEMATICAL MODELS

The relationship between relative permeability and resistivity index is derived in this section. The main theory behind this is the similarity between fluid flow in a porous medium and electricity flow in a conductive body.

2.3.1 Calculation of the Wetting-Phase Relative Permeability

The conductance of a porous medium at a water saturation of 100% is:

$$G_a = 1/R_o \tag{2.1}$$

where R_o is the resistivity at a water saturation of 100%, G_a is the conductance of a porous medium at a water saturation of 100%.

The conductance of a porous medium at a specific water saturation of S_w is:

$$G_w = 1/R_t \quad (2.2)$$

where R_t is the resistivity and G_w is the conductance at a specific water saturation of S_w .

According to the similarity theory between fluid flow and electric flow, the relative permeability of the wetting phase can be calculated using the following equation:

$$k_{rw} = \frac{G_w}{G_a} = \frac{R_o}{R_t} = \frac{1}{I} \quad (2.3)$$

where I is the resistivity index, k_{rw} is the relative permeability of the wetting phase.

According to Archie's equation (1942), the following equation applies:

$$I = \frac{R_t}{R_o} = (S_w)^{-n} \quad (2.4)$$

Where n is the Archie's saturation exponent.

At a water saturation of 100%, it is known that $I=1$, so the value of k_{rw} calculated using Eq. 2.3 would be equal to 1, which is true. At the residual water saturation, it is known that $k_{rw}=0$, which implies that I approaches infinity according to Eq. 2.3. But it is known that the value of I does not approach infinity at the residual water saturation. So the value of k_{rw} calculated using Eq. 2.3 is greater than zero, which is not consistent with physical observation.

One can also expect that the relative permeability of the wetting phase calculated using Eq. 2.3 will be greater than the true value. The reason is that the resistivity counts the average volumetric properties of the pore bodies in a porous medium while permeability counts the properties of pore throats. This is also why resistivity well logging can obtain porosity but not permeability.

Considering these problems, Eq. 2.3 is modified as follows:

$$k_{rw} = \frac{S_w - S_{wr}}{1 - S_{wr}} \frac{1}{I} \quad (2.5)$$

where S_{wr} is the residual saturation of the wetting phase. According to Eq. 2.5, $k_{rw}=1$ at $S_w=100\%$ and $k_{rw}=0$ at $S_w=S_{wr}$, which is reasonable.

Eq. 2.5 can also be expressed as follows:

$$k_{rw} = S_w^* \frac{1}{I} \quad (2.6)$$

S_w^* is the normalized saturation of the wetting phase and is expressed as follows:

$$S_w^* = \frac{S_w - S_{wr}}{1 - S_{wr}} \quad (2.7)$$

Relative permeability of the wetting phase can be calculated using Eq. 2.6 from resistivity index data once the residual saturation of the wetting phase is available. Note that the residual saturation of the wetting phase can be obtained from the experimental measurement of resistivity.

2.3.2 Calculation of the Nonwetting-phase Relative Permeability

According to Li and Horne (2002), the wetting-phase relative permeability can be calculated using the Purcell approach (1949):

$$k_{rw} = (S_w^*)^{\frac{2+\lambda}{\lambda}} \quad (2.8)$$

where λ is the pore size distribution index and can be calculated from capillary pressure data.

After the relative permeability curve of the wetting phase is obtained using Eq. 2.6, the value of λ can be inferred using Eq. 2.8.

According to the Brooks-Corey model (1964) and the study by Li and Horne (2002), the relative permeability of the nonwetting phase can be calculated once the value of λ is available. The equation is expressed as follows:

$$k_{rnw} = (1 - S_w^*)^2 \left[1 - (S_w^*)^{\frac{2+\lambda}{\lambda}} \right] \quad (2.9)$$

One can see that the entire relative permeability set (both wetting and nonwetting phases) can be inferred from resistivity index data using Eqs. 2.6 and 9.

2.4 RESULTS

The experimental data of resistivity and capillary pressure measured by Sanyal (1972) in rocks with different permeability were used to test the models (Eqs. 2.6 and 9) developed in this study. Firstly the values of relative permeability were calculated using Eqs. 2.6 and 9. Secondly relative permeability data were calculated using capillary pressure data (Li and Horne, 2002). According to the study by Li and Horne (2002), relative permeability could be calculated accurately using the capillary pressure technique. Finally the results of relative permeability inferred from resistivity index and capillary pressure data were compared.

2.4.1 Berea Sandstone

The Berea sandstone sample used by Sanyal (1972) had a porosity of 20.4% and a permeability of 300 md. Fig. 2.1 shows the relationship between resistivity index and water saturation in Berea sandstone at a temperature of 175°F.

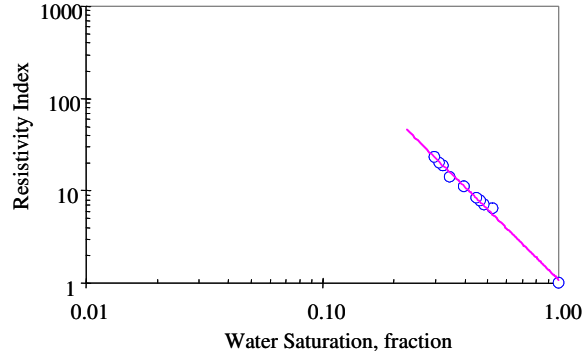


Figure 2.1: Relationship between resistivity index and water saturation in Berea sandstone at a temperature of 175°F (Sanyal, 1972).

The values of the resistivity index at different water saturation shown in Fig. 2.1 were measured in oil-water (water displaced by oil) systems. Fig. 2.1 also shows that the relationship between resistivity index and water saturation in Berea sandstone at a temperature of 175°F is linear on a log-log plot, which is consistent with Eq. 2.4.

Oil/water capillary pressure data were measured simultaneously with resistivity in the same core sample. The results are plotted in Fig. 2.2.

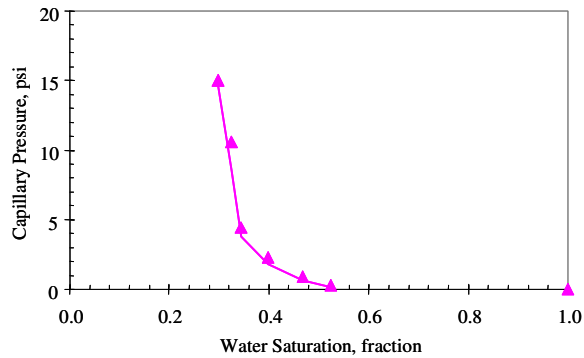


Figure 2.2: Capillary pressure data measured in Berea sandstone at a temperature of 175°F (Sanyal, 1972).

Oil/water relative permeability data were calculated from resistivity index (using Eqs. 2.6 and 9) and capillary pressure data (See Li and Horne, 2002) respectively. The results are compared and shown in Fig. 2.3.

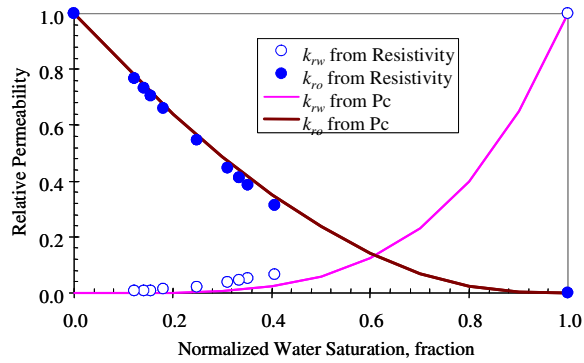


Figure 2.3: Relative permeability calculated from resistivity and capillary pressure data in Berea sandstone at a temperature of 175°F.

The results shown in Fig. 2.3 demonstrate that the relative permeability data inferred from the resistivity index data are close to those calculated using capillary pressure data. The oil relative permeabilities inferred from resistivity index data are almost equal to those calculated from capillary pressure data.

Sanyal (1972) also conducted the experimental measurements of resistivity index and capillary pressure at different temperatures in the same core sample. The resistivity index data at a temperature of 300°F are plotted in Fig. 2.4. One can see from Fig. 2.4 that the resistivity index data also follows the Archie's law (Eq. 2.4).

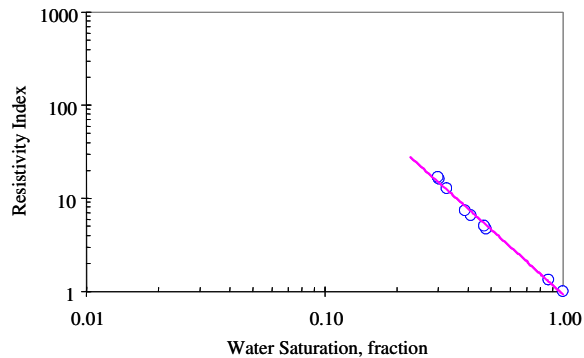


Figure 2.4: Relationship between resistivity index and water saturation in Berea sandstone at a temperature of 300°F (Sanyal, 1972).

Fig. 2.5 shows the oil/water capillary pressure data measured simultaneously with resistivity in the same Berea sandstone core sample at a temperature of 300°F.

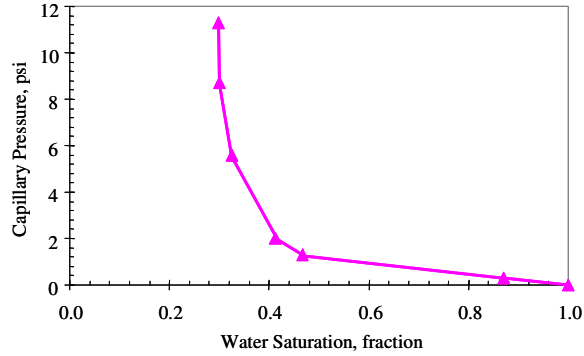


Figure 2.5: Capillary pressure data measured in Berea sandstone at a temperature of 300°F (Sanyal, 1972).

Fig. 2.6 demonstrates the relative permeability data calculated from both the resistivity index data shown in Fig. 2.4 (using Eqs. 2.6 and 9) and the capillary pressure data in Fig. 2.5 (see Li and Horne, 2002).

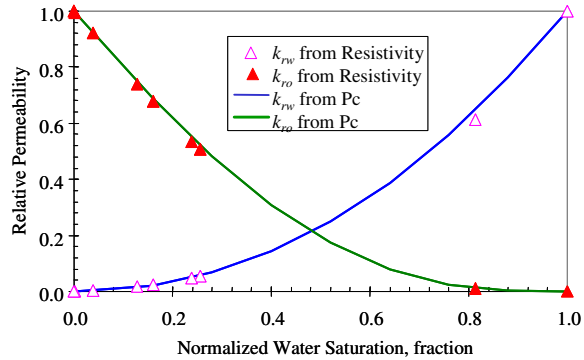


Figure 2.6: Relative permeability calculated from resistivity and capillary pressure data in Berea sandstone at a temperature of 300°F.

One can see in Fig. 2.6 that both the oil and water relative permeabilities inferred from the resistivity index data are almost equal to those calculated from the capillary pressure data.

2.4.2 Boise Sandstone

The Boise sandstone core sample had a porosity of 32% and a permeability of 960 md. The values of porosity and permeability are greater than those of Berea sandstone used by Sanyal (1972).

Figs. 2.7 and 8 show the resistivity index data and capillary pressure vs. water saturation in Boise sandstone at a temperature of 175°F.

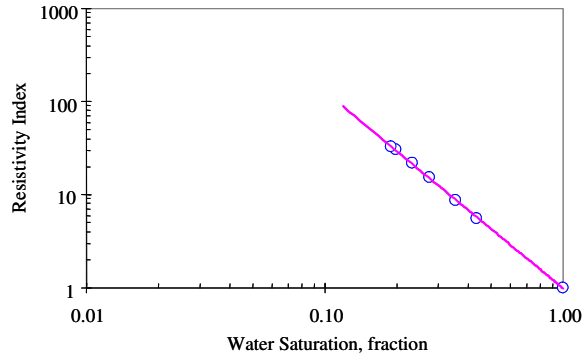


Figure 2.7: Relationship between resistivity index and water saturation in Boise sandstone at a temperature of 175°F (Sanyal, 1972).

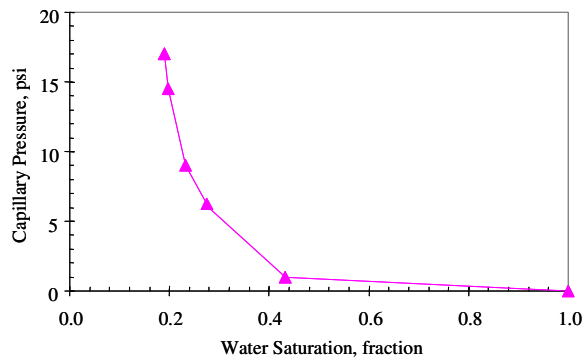


Figure 2.8: Capillary pressure data measured in Boise sandstone at a temperature of 175°F (Sanyal, 1972).

The relative permeability data calculated from both the resistivity index data shown in Fig. 2.7 (using Eqs. 2.6 and 9) and the capillary pressure data in Fig. 2.8 are plotted in Fig. 2.9.

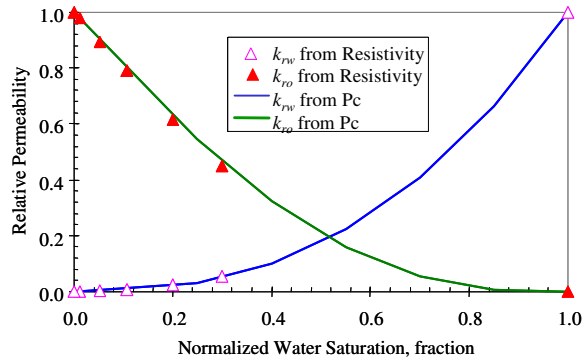


Figure 2.9: Relative permeability calculated in Boise sandstone at a temperature of 175°F.

Fig. 2.9 shows that the oil and water relative permeabilities calculated from the resistivity index data are close to those calculated from the capillary pressure data.

The results at a temperature of 300°F are demonstrated in Figs. 2.10-12. Fig. 2.10 shows the resistivity data and Fig. 2.11 shows the capillary pressure data. Fig. 2.12 plots the relative permeability calculated from the resistivity index shown in Fig. 2.10 (using Eqs. 2.6 and 9) and the capillary pressure in Fig. 2.11 respectively.

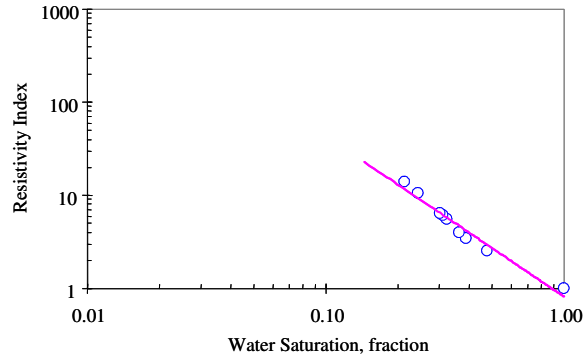


Figure 2.10: Resistivity index in Boise sandstone at a temperature of 300°F (Sanyal, 1972).

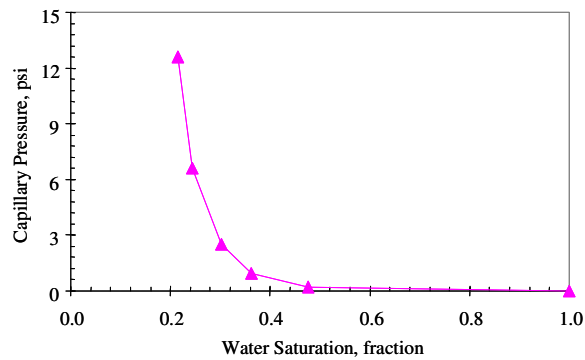


Figure 2.11: Capillary pressure data measured in Boise sandstone at a temperature of 300°F (Sanyal, 1972).

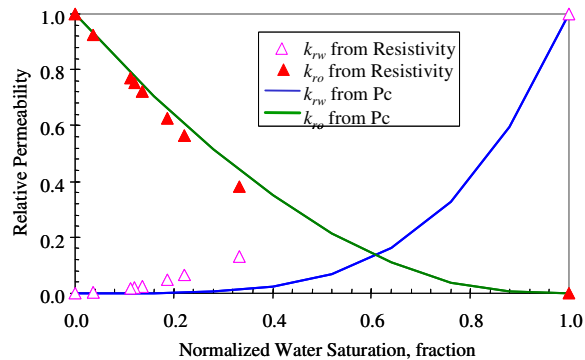


Figure 2.12: Relative permeability calculated from resistivity and capillary pressure data in Boise sandstone at a temperature of 300°F.

Fig. 2.12 shows that the oil relative permeability calculated from resistivity index is close to those inferred from capillary pressure. However the water relative permeability calculated from resistivity index data is smaller than those inferred from capillary pressure.

2.4.3 Limestone

The limestone core sample had a porosity of 19% and a permeability of 410 md. The resistivity index and capillary pressure data at a temperature of 300°F are displayed in Figs. 2.13 and 14 respectively.

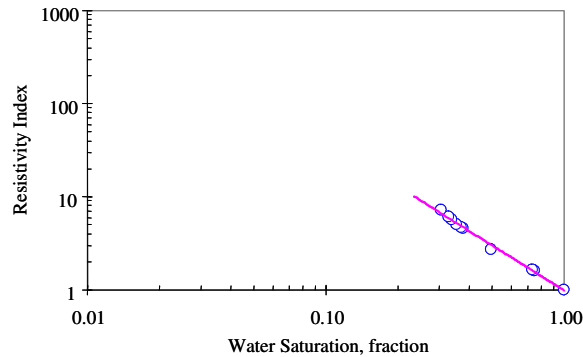


Figure 2.13: Resistivity index vs. water saturation in limestone at a temperature of 300°F (Sanyal, 1972).

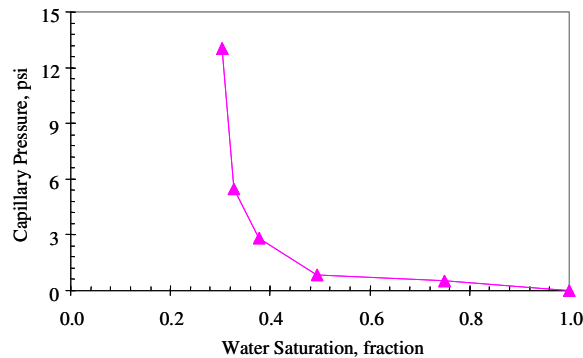


Figure 2.14: Capillary pressure data measured in limestone at a temperature of 300°F (Sanyal, 1972).

The results of relative permeability calculated from the resistivity index and the capillary pressure data are shown in Fig. 2.15.

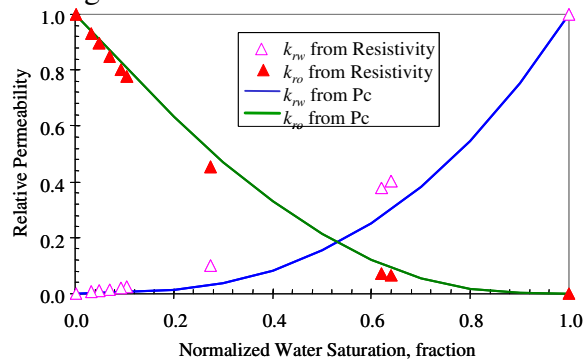


Figure 2.15: Relative permeability calculated from resistivity and capillary pressure data in limestone at a temperature of 300°F.

One can see in Fig. 2.15 that the oil relative permeabilities inferred from the resistivity index data are almost equal to those calculated from the capillary pressure data in limestone core sample. The difference between the relative permeability inferred from the resistivity index and those calculated from capillary pressure is acceptable in terms of reservoir engineering applications.

2.5 CONCLUSION

Based on the present study, the following conclusions may be drawn in the cases studied:

1. A semianalytical model was developed to infer relative permeability from resistivity index data.
2. The values of the nonwetting phase relative permeability inferred from the resistivity index data are almost equal to those calculated from capillary pressure data.
3. For the wetting-phase relative permeability, the values inferred from the resistivity index are close to those calculated from capillary pressure in most of the cases studied.

3. FRACTURED ROCK RELATIVE PERMEABILITY

This project is being conducted by Research Assistant Anson L. Villaluz, Senior Research Engineer Kewen Li and Prof. Roland N. Horne. The objective is to obtain measurements of steam-water relative permeability in real fractured rocks from geothermal reservoirs. This work is an extension of our earlier steam-water relative permeability studies which have mostly considered artificially uniform and high permeability rocks. Now that the relative permeability mechanisms have been understood, we are working on the more difficult measurements using heterogeneous, low permeability rocks from geothermal reservoirs.

3.1 BACKGROUND

Steam-water relative permeability and capillary pressure are important data for geothermal reservoir engineering. The Stanford Geothermal Program (SGP) has succeeded in making fundamental measurements of steam-water flow in porous media and made significant contribution to the industry. One of the important problems left to undertake is the measurement of steam-water relative permeability and capillary pressure in geothermal rock (most of the previous study was conducted in high permeability sandstone as a well-controlled test material.).

Using our existing steady-state CT method, we have measured steam-water relative permeability and capillary pressure in rock with permeability above 1 md (10^{-13} cm²). We can obtain the in-situ fluid saturation simultaneously. For the geothermal rock with permeability smaller than 1 md (10^{-13} cm²), the steady-state CT method would work but it would take an extremely long time to conduct the experiments (weeks or even months). Hence the CT method is not practical to measure steam-water relative permeability in geothermal rocks.

To overcome this difficulty, we have undertaken a different approach, by measuring the relative permeability curves in separate sections. We have concluded from our experimental data (Satik, 1998; Horne *et al.*, 2000; Mahiya, 1999; O'Connor, 2001; Li and Horne, 2000a) that steam-water relative permeability follows the Corey model and steam-water capillary pressure follow the Brooks-Corey model. We can measure the end-point steam-water relative permeability and saturation in the geothermal rock with permeability smaller than 1 md using our existing steady-state CT method or the direct weighing method developed by Li *et al.* (2001). Then the whole curve of steam-water relative permeability can be obtained using the Corey model and the capillary pressure curve can be obtained using the Brooks-Corey model. We plan to confirm the applicability of this approach first with nitrogen-water experiments, which are very much easier to conduct than the steam-water flows. This work was begun by Habana (2002), but ran into experimental difficulties.

The experimental study performed by Habana (2002) on a real fractured geothermal core showed results with pressure spikes occurring periodically during single-phase water injection. Erratic pressure spikes were observed during nitrogen-water relative permeability experiment in the same study. Some of the results are presented in Figures 3.1 and 3.2. The appearance of these transient effects indicated a difficulty with the

experimental configuration, and prevented the measurement of relative permeability. In the continuation of this study, the apparatus will be redesigned and reconstructed to overcome these problems.

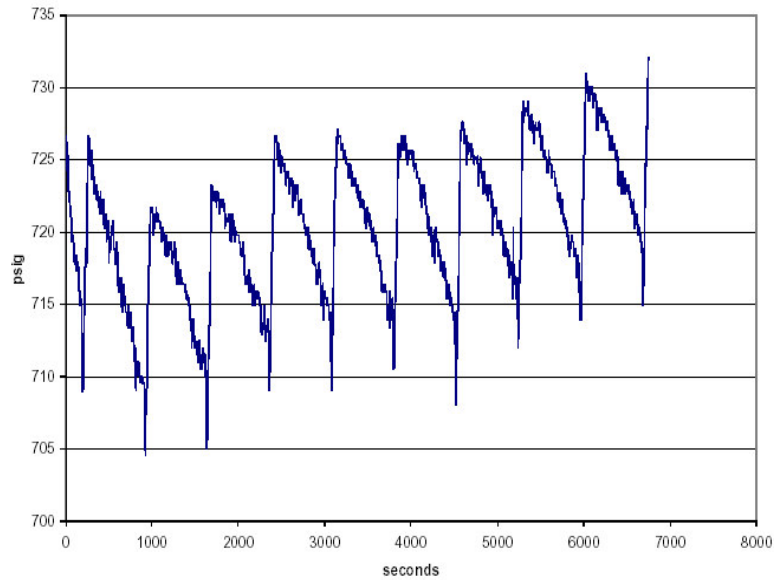


Figure 3.1: Pressure at inlet during water injection. Constant water flow rate at 14 ml/min (Habana, 2002).

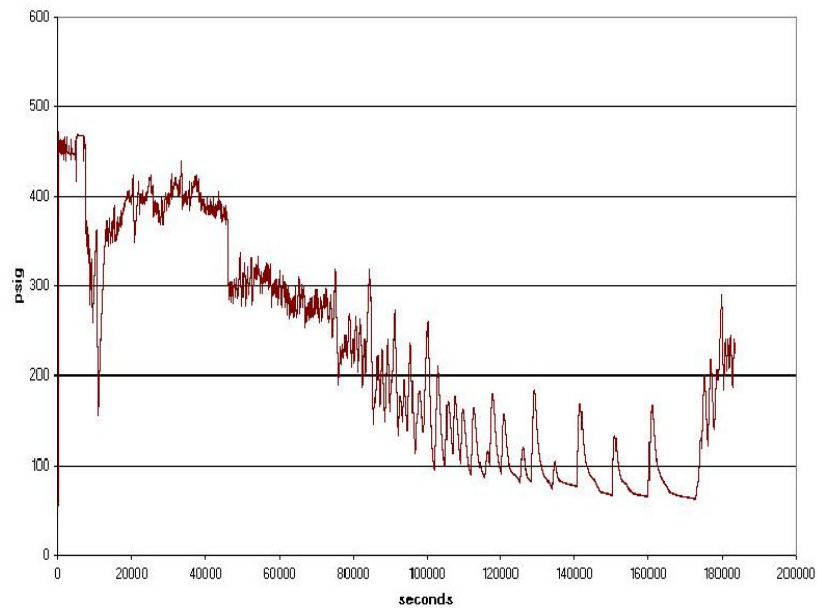


Figure 3.2: Pressure at inlet for constant flow rate nitrogen-water experiment (Habana, 2002).

3.2 EXPERIMENTAL METHODOLOGY

The rock permeability will be measured using nitrogen gas at room temperature. Gas permeability is a function of pressure. Therefore, the flow measurements will be conducted at a series of different mean pressures and taking into account Klinkenberg slip effect.

A new core sample has been obtained from a depth of 2440.5m at The Geysers geothermal field. The core is 4.71 cm in length and 2.72 inches in diameter. Pore volume of the core is measured to be 3.02 cc and porosity is calculated to be 1.7 %. Pore volume and porosity were measured by drying the core under vacuum at 110°C, after which further evacuating was done using a vacuum pump. The core was then saturated with deionized water and weighed to determine amount of water impregnated.

Nitrogen will be flowed into the core at different confining pressures. Confining pressure from 500 to 850 psig can be reached by injecting nitrogen around the heat shrink tubing inside the core holder. To apply higher confining pressure water will be used in place of nitrogen.

A schematic illustration of the experiment is shown in Figure 3.3.

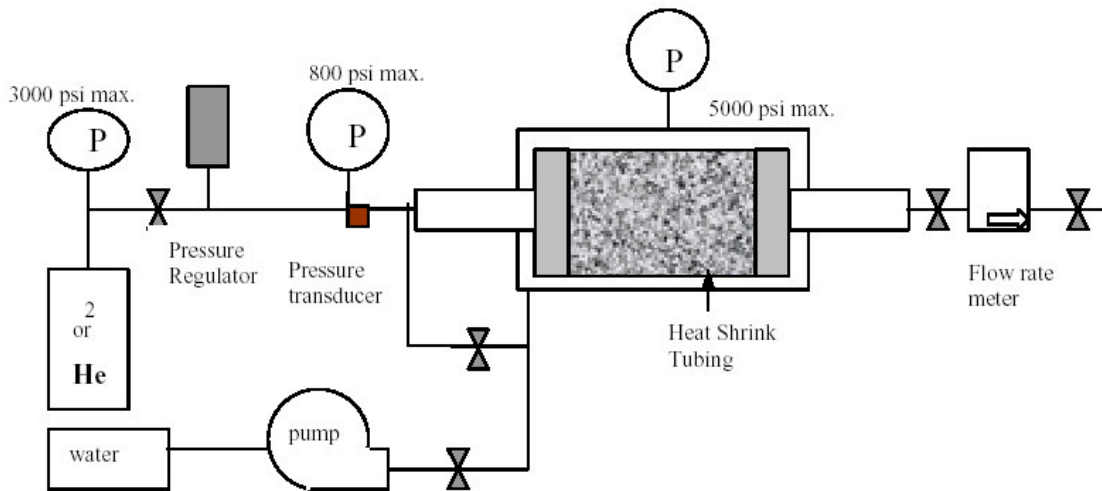


Figure 3.3: Schematic representation of apparatus

The apparatus was set up and leak test was performed, leak problems were encountered using shrink tubing to compartmentalize the core from the confining pressure. Epoxy will be used to provide complete sealing and to prevent leaks through the end plates.

3.3 THEORETICAL BACKGROUND FOR ELECTRICAL RESISTIVITY

Electrical resistivity measurements were obtained to validate relationship of resistivity with saturation via Archie's Equation.

This relationship can be represented by Equation 3.1:

$$I = bS_w^{-n} \quad (3.1)$$

where $I = R_t/R_o$ known as the resistivity index, R_t is the resistivity at a certain saturation, R_o is the resistivity at 100% water saturation, b is some function of tortuosity, and n is the saturation exponent. Empirically, $n=2$ for Berea sandstone from previous studies.

3.4 NITROGEN-WATER RELATIVE PERMEABILITY EXPERIMENTAL METHOD

As a preparation to doing relative permeability measurements of geothermal core, and to have a deeper understanding of the relative permeability experimentation process, an apparatus was set up that is able to measure critical data to calculate for relative permeability.

The steady state method for obtaining relative permeability data was employed. 1% NaCl solution and nitrogen gas were used as the two phases entering the core. A schematic diagram for the apparatus is presented in Figure 3.4. Electrical resistivity measurements are taken simultaneously using an ordinary multimeter.

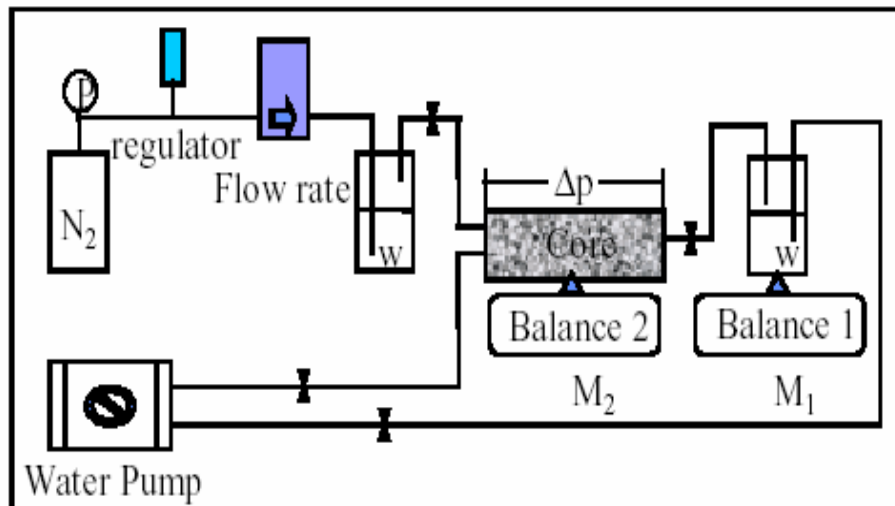


Figure 3.4: Schematic diagram of steady state N_2 - H_2O relative permeability test

Last time, the core was put inside a rubber sleeve and two layers of shrink tubing were further placed atop to prevent leak, but after some time, leaks were again observed. This time, an aluminum core holder was used to be able to apply confining pressure and to eliminate leaks.

Saturation data were measured by weighing the core using Balance 2 as shown in Fig. 3.4 and verified using mass balance through Balance 1.

3.5 NITROGEN-WATER RELATIVE PERMEABILITY RESULTS IN BEREA SANDSTONE

Using Darcy's Law and assuming that the ideal gas equation applies, effective permeability data were calculated at different saturation points.

As in a usual steady state relative permeability measurement, saturation was altered by adjusting relative injectivity, which is basically the ratio between the flow rates of brine and nitrogen entering the system.

The results of the relative permeability experiment are presented in Figure 3.5.

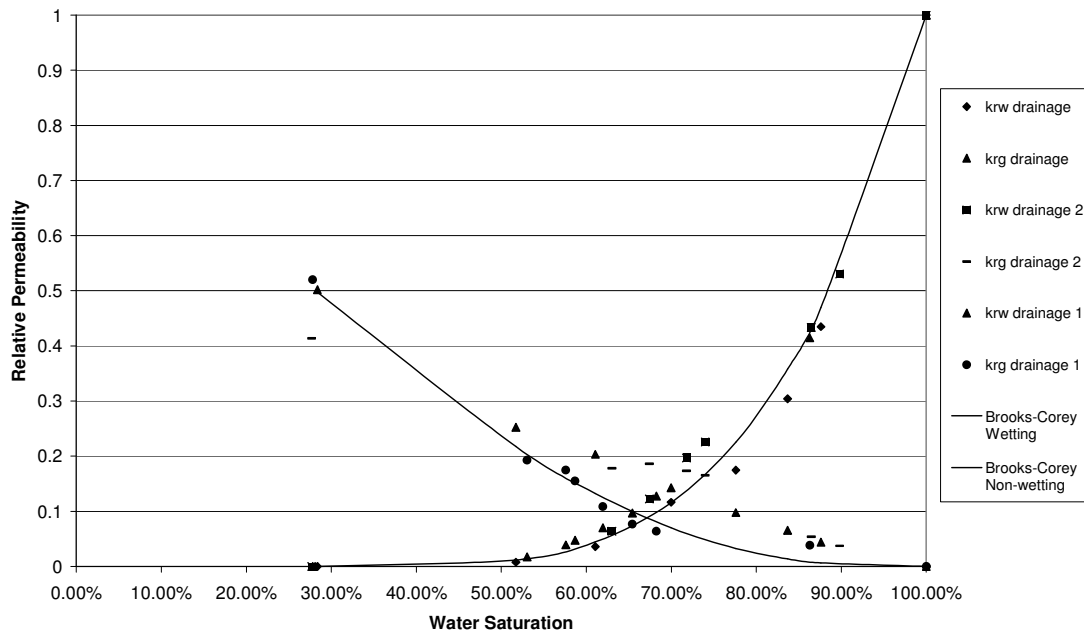


Figure 3.5: Nitrogen-Water Drainage Relative Permeability in Berea Sandstone

Figure 3.5 shows a summary of three drainage relative permeability experiments done with Nitrogen and 1% NaCl solution using Berea Sandstone. To explain the legend, *krw* drainage, *krg* drainage, *krw* drainage 1 and *krg* drainage 1 were done with the improved core holder. *Krw* drainage 2 and *krg* drainage 2 were results presented in the April-June 2004 Quarterly Report (Fractured Rock Relative Permeability).

The general trend of the results seen in Figure 3.5 is acceptable. Relative permeability of a particular phase increases as saturation of that particular phase increases and vice versa.

Plotted against a semiempirical model, the results can be observed generally to follow the Brooks-Corey series model (with $\lambda=2$).

Meanwhile, Figure 3.6 summarizes relative permeability measurements obtained during imbibition. Comparing Figure 3.5 with Figure 3.6, it can be seen that relative permeability of the nonwetting phase during imbibition is less than during the drainage process due to nonwetting phase trapping. On the other hand, the effect of saturation history to the wetting phase was observed to be not considerable, as expected. The results for kr_w imbibition 2 and kr_g imbibition 2 were not included in Figure 3.6 since that experiment suffered from leaks and unrealistically low relative permeability values were therefore obtained.

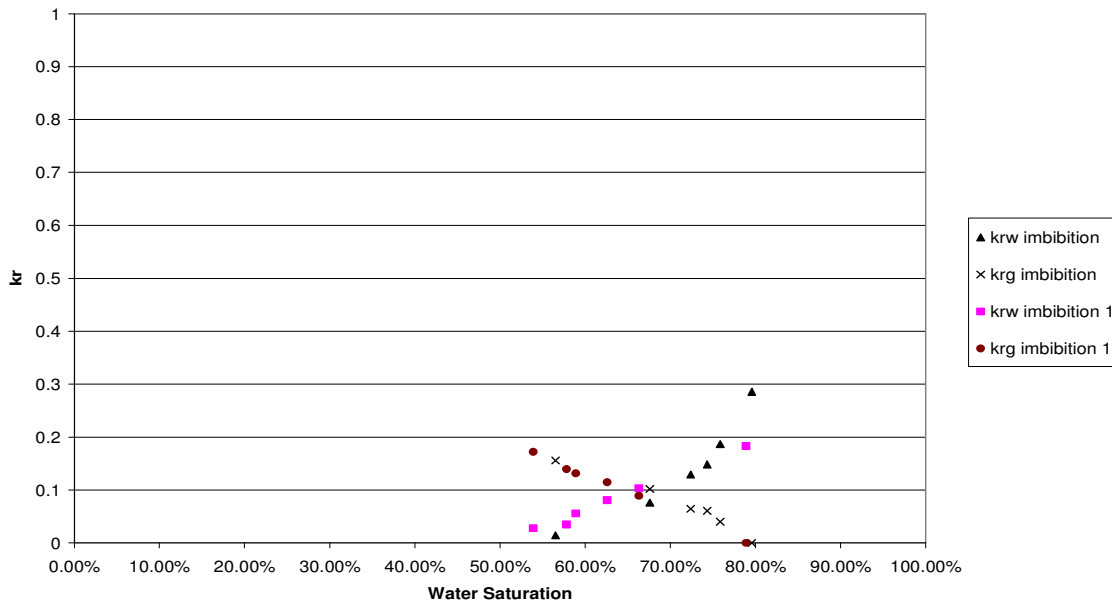


Figure 3.6: Nitrogen-Water Imbibition Relative Permeability in Berea Sandstone.

3.6 RESULTS OF ELECTRICAL RESISTIVITY IN RELATIVE PERMEABILITY MEASUREMENTS

The result of using Archie's equation to correlate electrical resistivity with saturation while doing nitrogen-water relative permeability experiment is presented in Figure 3.7. An AC Meter was used for this purpose and the results seem to be better than those obtained using a DC Multimeter (April-June 2004 Quarterly Report Fractured Rock Relative Permeability). 100 Hz was chosen among the range of frequencies because it was found out that the phase shift of the current when applied to the system is least on this frequency. This usually gives the most accurate resistance readings on practice.

It can be observed from Figure 3.7 that Archie's correlation seems to work well during both drainage and imbibition processes. One thing noteworthy is that the cementation factor is higher (about 5.4) than that of the usual Berea sandstone (about 2). This can be attributed to the firing of the Berea sandstone used in the experiment. During the firing

process, clays (which are conductive materials) are calcified, therefore, decreasing the overall conductivity of the material and increasing its resistance/resistivity.

Another interesting observation from Figure 3.7 is that the resistivity indices are sensitive to the flow history, for the imbibition process indices are lower than that of the drainage process. This may be due to the fact that during drainage, the dominant flowing fluid is gas which has relatively low conductivity while during imbibition, brine is the dominant flowing fluid.

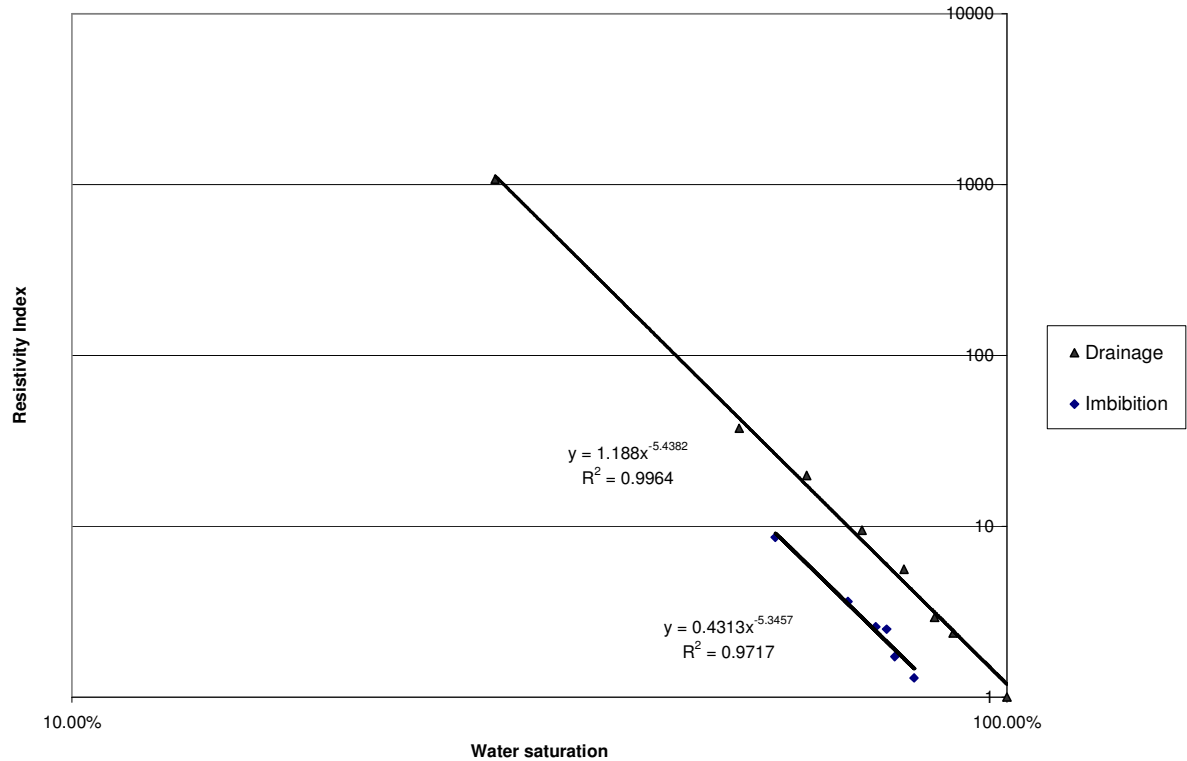


Figure 3.7: Archie's Correlation using 100 Hz AC Frequency

3.7 ELECTRICAL RESISTIVITY RESULTS IN GEOTHERMAL ROCK

Electrical resistivity measurements vs. saturation were investigated because the resulting model will be useful while performing relative permeability measurements to calculate saturation without using the direct weighing method, and to validate results from saturation calculations from mass balance.

The experiment was performed by allowing the saturated geothermal rock to evaporate naturally while taking measurements of weight and resistivity as time progressed. This experiment lasted for 24 hours until accurate measurement of resistivity could no longer be taken, probably due to drying of the core ends. Consequently, the lowest saturation value measured was not able to be taken lower than 60% using this method.

Results of resistivity measurements for different AC frequencies are presented in Figures 3.8, 3.9, 3.10 and 3.11. Resistivity can be seen to increase with decreasing saturation for all cases. Comparing the four figures, it can be observed that using a frequency of 10 kHz yields the best fit for Archie's correlation.

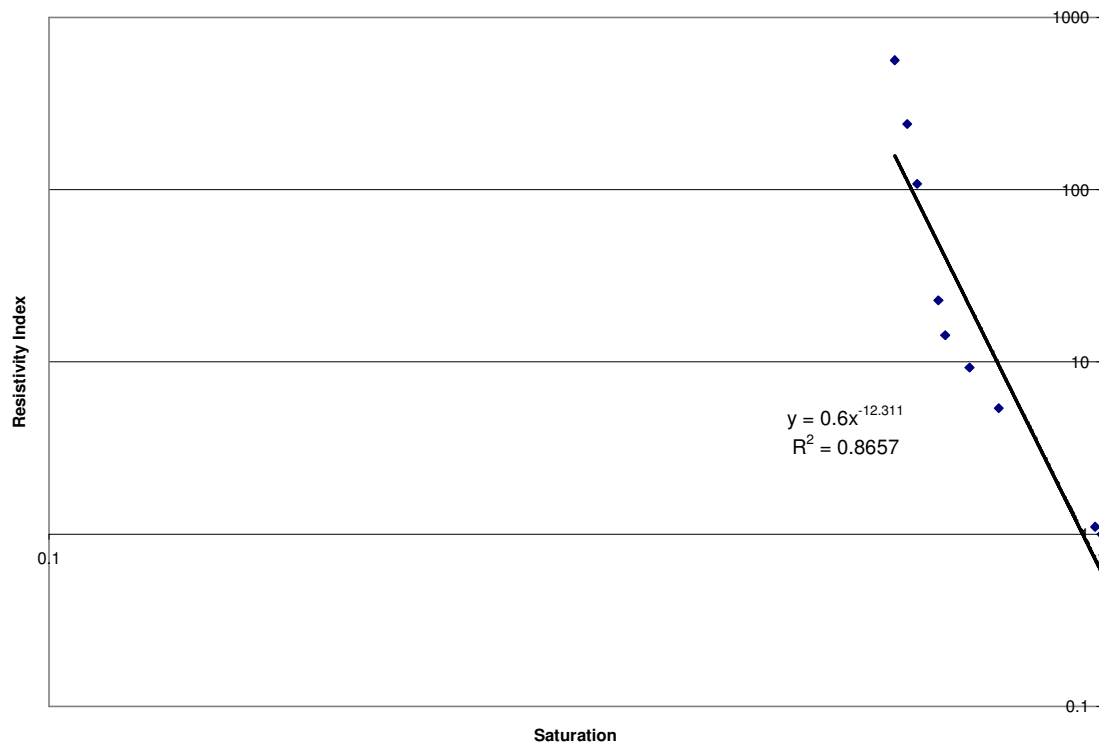


Figure 3.8: Archie's Correlation using 100 Hz AC Frequency.

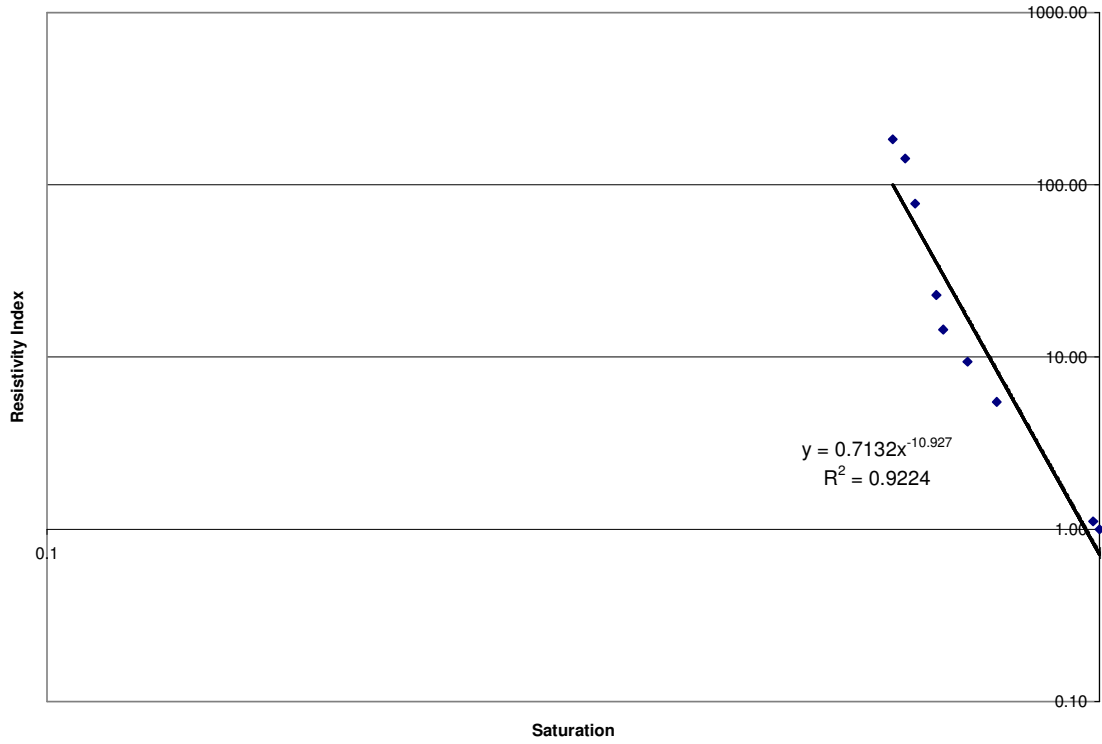


Figure 3.9: Archie's Correlation using 1 kHz AC Frequency.

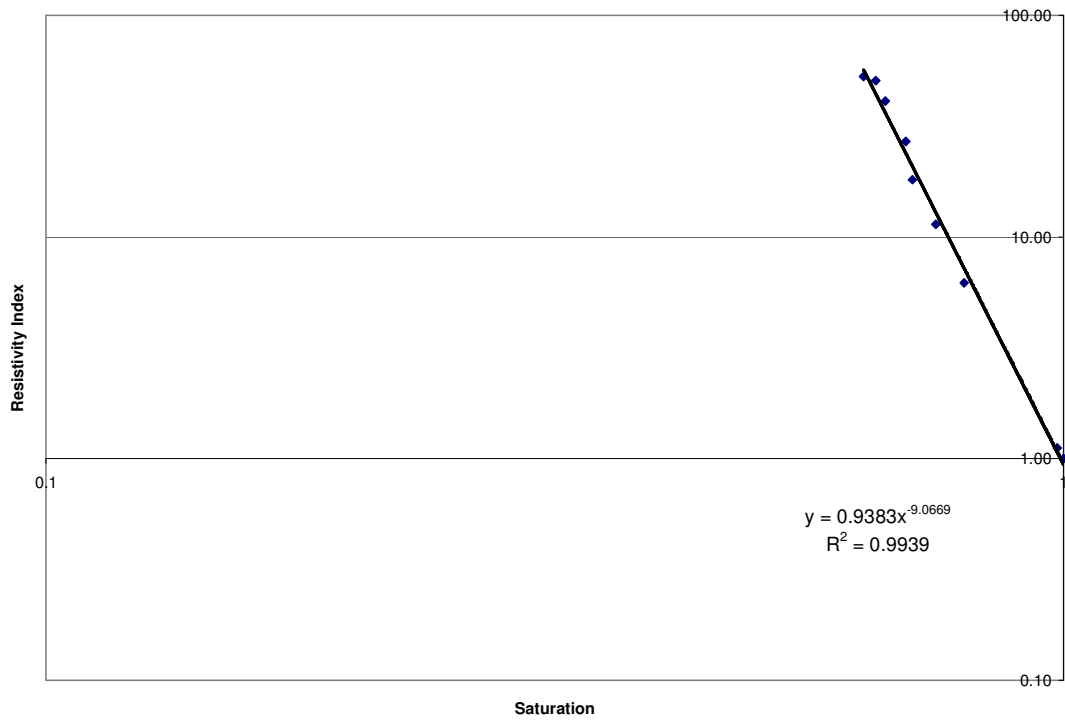


Figure 3.10: Archie's Correlation using 10 kHz AC Frequency.

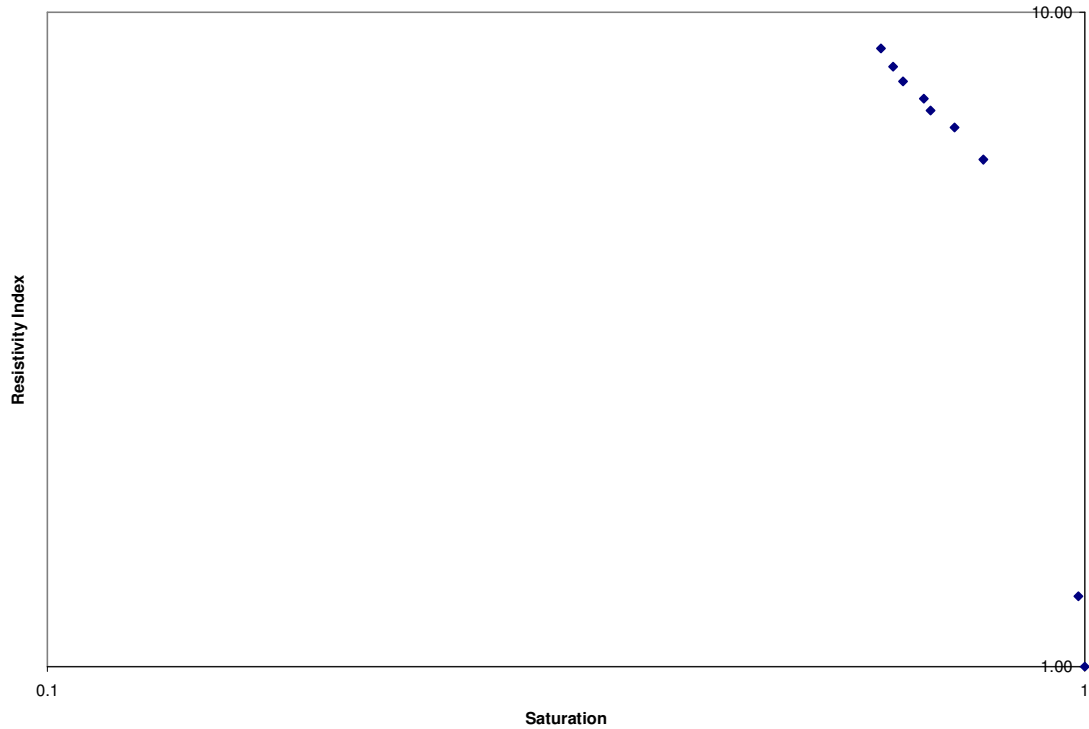


Figure 3.11: Archie's Correlation using 100 kHz AC Frequency.

3.8 CONTINUING AND FUTURE WORK

The core holder used by a past researcher, Mark Habana, is being used, with some modifications. Currently, leak tests are being conducted and hopefully leaks will be prevented by application of epoxy to the leak prone zones, especially between the end plate and the shrink tubing.

After leak testing, permeability of the rock will be measured using nitrogen. Nitrogen-water as well as steam-water relative permeability measurements will then be conducted. Current relative permeability models will be tested against the experimental data obtained.

Lastly, the application of pore network modeling with the aim of deriving relative permeability curves of fractured rocks will also be investigated to verify results from the fractured rock experiment.

4. ELECTRICAL IMPEDANCE TOMOGRAPHY (EIT) METHOD FOR SATURATION DETERMINATION

This research project is being conducted by Research Assistant Robert Stacey, Senior Research Engineer Kewen Li and Prof. Horne. The intent of this project is to develop a method to measure core saturation using electrical impedance tomography (EIT). This method is being investigated because the CT scan technique has limitations on pressures and temperatures due to the strength of the plastic core holders available.

4.1 INTRODUCTION

The idea to measure the saturation distribution in a core using EIT was described in a paper by Van Weereld, et al. (2001). The paper showed that EIT techniques were able to measure the saturation of a two phase system (oil and brine) nearly in real time. Therefore this method is being investigated further in order to better understand two-phase (steam water) systems.

4.1.1 Background

The idea behind EIT is that by imposing an electric current across an inhomogeneous medium, the distribution of the internal electrical impedance will give rise to a variation of voltage potential at the surface. Measurements of the variable voltage potential could be used to infer the resistivity distribution within the medium. This internal distribution of electrical impedance then can be translated into water saturation based upon the impedance distinction between the two phases. Figure 4.1 is a diagram of a typical two-dimensional EIT experiment, consisting of 16 electrodes with an imposed current I across the core Ω , and measurement of the resulting potential V_1 .

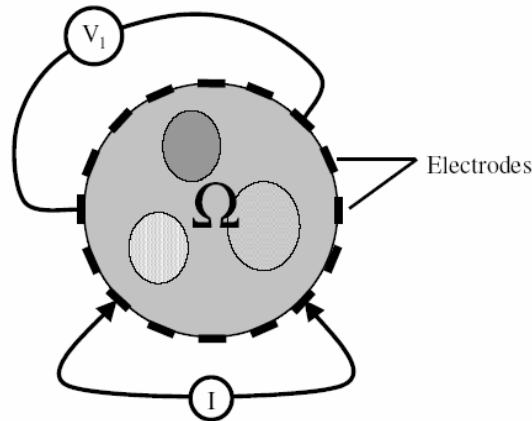


Figure 4.1: Diagram of Electrical Impedance Tomography experiment. The potential V_1 is measured after a current I has been imposed across the core Ω . (Molinari 2003)

The governing equation for EIT imposed upon a core Ω is

$$\nabla \cdot (\sigma + i\omega\epsilon)\nabla\phi = 0 \quad (4.1)$$

Where σ is the electric impedance of the medium, ϕ is the electric potential, ω is the frequency, and ϵ is the electric permittivity. Under conditions where low frequency or direct current is used ($\omega \approx 0$), Equation 4.1 can be reduced to the standard governing equation for EIT (Molinari 2003):

$$\nabla \cdot (\sigma \nabla \phi) = 0 \quad (4.2)$$

The EIT inverse problem can be simplified down to a system identification problem. The cause and effect (injected current I and measured voltage V) are known, but the physical system is unknown (impedance distribution σ). The nonlinearity arises in σ , as the potential distribution ϕ is a function of the impedance, $\phi = \phi(\sigma)$, and we cannot easily solve Equation 4.2 for σ (Molinari 2003). The ill-posed nature of the problem is clearly apparent when observing the diffusive nature of electricity, coupled with the inherent measurement errors.

4.1.2 Research

The areas required to develop an effective EIT system can be separated into three main categories; electrode configuration and connection, data acquisition, and data processing. The latter two have been researched and developed in similar fields, particularly the medical field. Polydorides (2002) in particular has worked extensively in addressing the data processing issue of soft-field tomography, and has developed a MATLAB toolkit EIDORS exclusively for this problem.

The Electrical Impedance and Diffuse Optical Reconstruction Software (EIDORS) project has developed a community that promotes communication and sharing of software to further the development of EIT. The software, documentation, demonstrations and available help will be useful when data processing and volume visualization begins in this project.

As for the data acquisition system, the experiment of Weerld et al. (2001) required collecting data from 192 electrodes simultaneously to produce near real-time images, and did so successfully. However, the optimum order and procedure in collecting data has been debated by Molinari (2003) and Polydorides (2002), both of whom have modeled the system at hand extensively, but have performed little physical experimentation. Polydorides (2002) has suggested that a 16 electrode ring is the optimum size based upon computational time, the noise imposed by additional electrodes, and the fraction of singular values that are useful. Another method of interest suggested by Polydorides (2002) is a segmented electrode configuration. For example four electrodes across from one another would be turned on simultaneously, while the remaining electrodes measure voltage independently. Molinari (2003) and Polydorides (2002) have many suggestions on techniques to reduce computational time, increase resolution, and filter out noise, but all of this will be applied and discussed in greater detail when data acquisition begins.

The major foreseen difficulty is in the electrode configuration and connections. In several papers (Van Weereld et al., 2001, Polydorides 2002, and Molinari 2003) it has been found that accurate, consistently geometric connections are difficult to obtain, and the practical

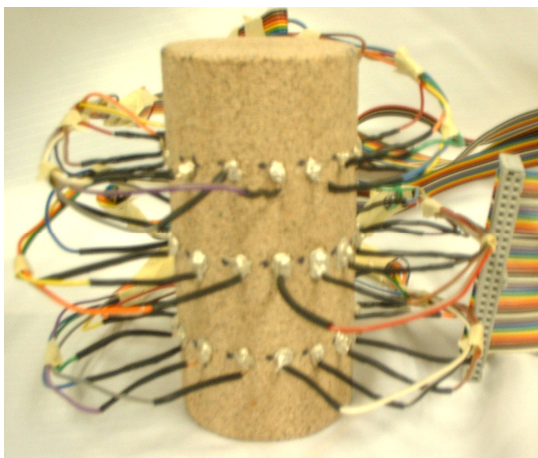
limitations imposed by wiring limit the number attached by hand (Van Weereld et al. 2001). A solution to this problem was to use a flexible circuit designed for the core specifically to ensure consistent size and distribution of electrodes while also creating a compact manageable system as compared to conventionally wired electrodes. However, to begin the research a conventional wiring scheme has been used to begin testing some of the data collecting and processing schemes.

4.2 THE EIT APPARATUS

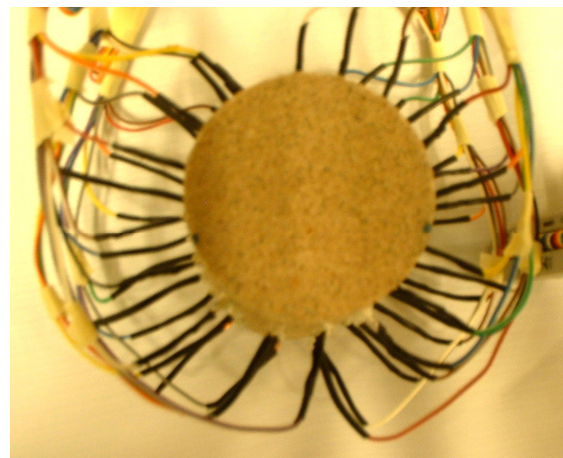
The primary idea behind the EIT apparatus, more specifically the electrode configuration, is that solid connections to the core sample must be made and the electrodes must be equidistant around the circumference of the core. This is in order to simplify the model used in solving the inverse problem. The design variations of the apparatus appear when trying to decide on a feasible number of electrodes, whether a flexible circuit is warranted and viable, and which design will be simple and reliable.

4.2.1 Preliminary Design

The preliminary design decided upon is simple enough to eliminate many unnecessary problems, such as leaks from the system, short circuiting, and bad connections. Yet the system is large enough with 3 rings of 16 electrodes to test the data acquisition system and the MATLAB toolkit EIDORS in post processing. Figure 4.2 shows the preliminary design with 3 rings of 16 electrodes attached to the Berea sandstone core with conductive epoxy. This design will work by placing the base of the sandstone into water and allowing water to naturally imbibe by capillary forces. During this time the data acquisition system will be recording the field potential and calculating the internal impedance distribution. The idea is that visual observations of the saturation front can be used in assessing the EIT system and its performance.



(Side View)



(Top View)

Figure 4.2: Side and top view of Preliminary Design. 48 electrodes were attached to a Berea sandstone core using conductive epoxy.

4.2.2 Future Design

If the preliminary design is successful in proving that it is feasible to determine saturation with EIT, then the project will move forward to one of the mentioned future designs. The two foreseen options will allow for high pressure and temperature conditions along with pressurized phase transport through the core, just as in typical core experiments. However, the main point at which the designs diverge is whether to use a flex circuit design or a modified rubber sleeve design. These two options will be investigated as research continues.

4.3 CONTINUING AND FUTURE WORK

Currently the data acquisition system is being developed for the EIT system, and upon completion we will begin performing our first saturation measurements using the EIT technique. It is anticipated that many unforeseen errors will appear along the course of developing this technique, but literary research has revealed that promising results are possible.

5. MEASUREMENTS OF IN-SITU WATER SATURATION IN DIFFERENT GEOTHERMAL ROCKS

This research project is being conducted by research assistant Aysegul Dastan, Senior Research Engineer Kewen Li and Prof. Horne. The objective is to study the effects of pressure, temperature and permeability on in-situ water saturation in geothermal reservoirs.

5.1 SUMMARY

Through an earlier project supported by the California Energy Commission (CEC) project, preliminary measurements were conducted, and rock from The Geysers was characterized experimentally (Horne et al. (2003)). Our objective is first to repeat these measurements, modifying the setup as necessary and next to carry out similar measurements in other geothermal rocks, in order to characterize the stored water characteristics of different geothermal fields..

5.1.1 Characterization of the rocks: S_w and ϕ parameters

The characterization uses computer tomography (CT) images of a rock sample under various pressure and temperature conditions. The objective is to determine the saturation and porosity values experimentally, represented as S_w and ϕ , respectively. Equations 5.1 and 5.2 relate these quantities to CT measurements.

$$S_w = \frac{CT_{exp}(T) - CT_{dry}(T)}{CT_{wet}(T) - CT_{dry}(T)} \quad (5.1)$$

$$\phi = \frac{CT_{wet}(T) - CT_{dry}(T)}{CT_{water}(T) - CT_{air}(T)} \quad (5.2)$$

In Equations 5.1 and 5.2, $CT_{wet}(T)$, $CT_{dry}(T)$ are CT values of the core sample when it is completely saturated by water and steam, respectively. $CT_{exp}(T)$ is the CT value when it is partially saturated by steam. CT_{water} and CT_{air} are the CT numbers of water and air, respectively.

5.1.2 Experimental Configuration

To measure the required parameters using the CT scanner, an experimental apparatus was built to bring the core to the desired temperature and pressure conditions and apply or drain water as necessary to achieve the ‘dry’ and ‘wet’ states. The core is placed in a core holder, as shown in Fig. 5.1. The core is machined and inserted in an aluminum cylinder filled with high-temperature epoxy, which is then cured at 160°C. To control the temperature in the core, an oil bath is used. The oil with a controlled temperature is passed through an external aluminum coil around the core holder.

The apparatus is shown in Fig. 5.2. In the configuration, the core holder is used with a vacuum system, a water pump, and a flow-rate controller. A set of pressure transducers and thermocouples are used with the system to monitor the pressure and the temperature at various points. It is possible to make the necessary adjustments for the desired

performance using the transducer readings that are conveniently displayed on the computer. Sensor readings are displayed and analyzed on a desktop computer using a LabView program.

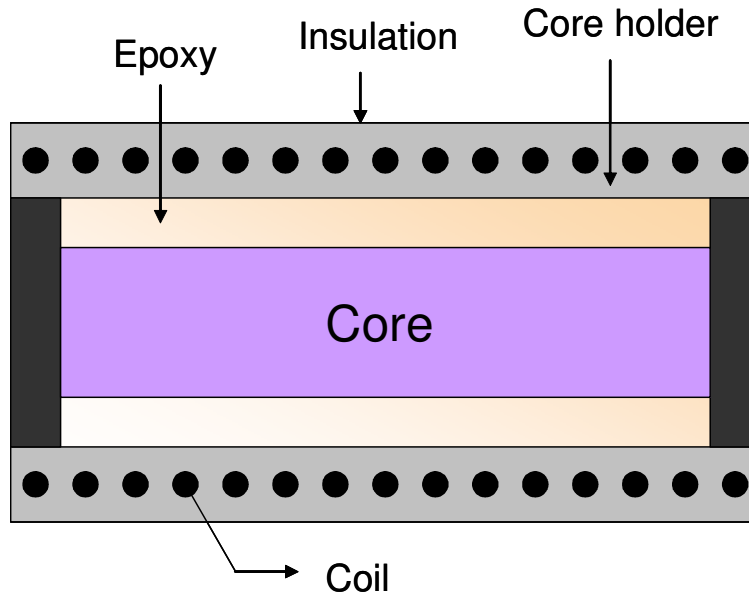


Figure 5.1: The core holder.

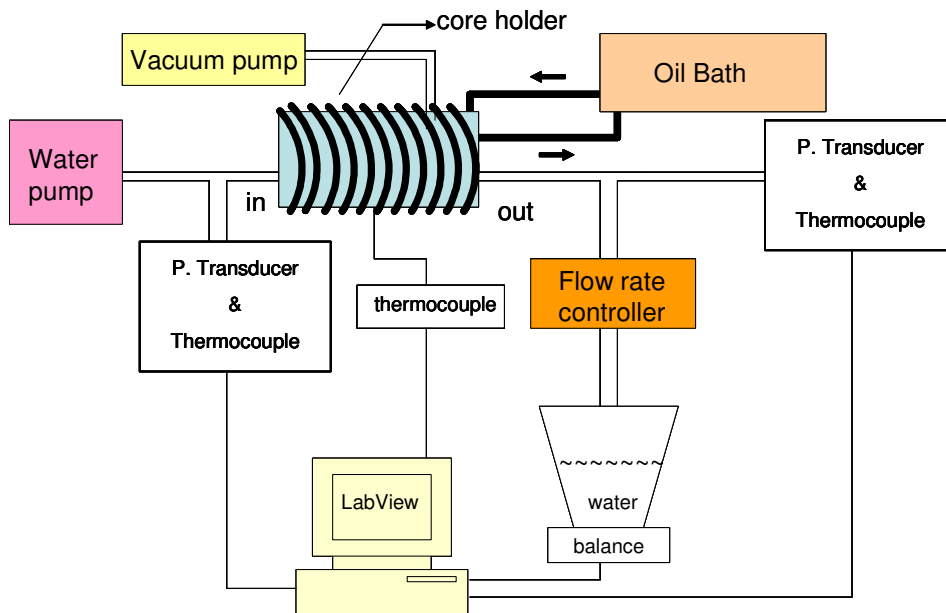


Figure 5.2: Experimental apparatus.

In the apparatus, the vacuum pump is used to remove the air in the core sample such that a steam-water environment can be established. Water is delivered using a water pump. The amount of the water delivered and leaving the sample can be recorded in the computer using an interface.

Note that the coil and the insulating material that is wrapped over the core holder are transparent to the X-rays emitted by the CT scanner.

5.1.3 Measurement Procedure

Our aim is to measure the CT_{dry} , CT_{wet} , and the CT_{exp} values that are needed to calculate the S_w and ϕ parameters through Equations 5.1 and 5.2. For that, first the core holder is dried by heating it to a temperature of ~ 120 °C and imposing a vacuum for ~ 48 hours. CT measurement gives the CT_{dry} value. Next, the core is saturated with water under vacuum after the sample is cooled down to room temperature. To ensure that the sample is saturated with water completely, a pressure of ~ 75 psi is applied sufficiently long. The temperature can now be elevated up to ~ 120 °C to obtain the CT_{wet} measurement. The temperature and the pressure can be varied to obtain a data set with respect to these parameters.

5.2 CURRENT STATUS

The existing apparatus from the CEC experiment has been analyzed component by component and the nonfunctional components have been replaced. Also the LabView program used to monitor the data has been reviewed, and all the transducers and the thermocouples have been calibrated to ensure that the readings on the computer reflect the actual values on the transducers. The valves and flowlines have been tested and it has been ensured that there is no leakage in the system. The oil-heating system has been tested for functionality and integrity with the rest of the system. Currently, the core holder holds a sample of The Geysers rock, which was previously characterized by Horne et al. (2003). The core has been dried and subjected to a vacuum, and the sample is ready for the CT_{dry} measurement. A new CT scanner is now available for use, and following a training period, it will be possible to repeat the experiment for The Geysers rock.

5.3 CONCLUSIONS

We have analyzed and completed the necessary maintenance for the existing experimental apparatus to be used for the characterization of The Geysers rock. Since this sample was characterized before, it will be useful to compare the two measurements to confirm the repeatability of the experiments. That will confirm that the apparatus works well with all the new adjustments and modifications. Following that, new geothermal rock samples will be analyzed. For that, new core holder assemblies will be prepared using appropriate epoxy filling material. Note that the temperature and pressure at which the data is taken will have to be adjusted according to the permeability of the samples. In the long run, these new data will be used to simulate the geothermal rocks from a given geographical location.

6. DOWNHOLE ENTHALPY MEASUREMENT

This research project is being conducted by Research Assistant Egill Juliusson and Professor Roland Horne. The objective of this project is to find a way to measure enthalpy downhole either by constructing a device specifically for that purpose or expanding the use of existing measurement technologies.

6.1 SUMMARY

Enthalpy is a measurement of combined internal and compressive energy of a fluid. Measuring enthalpy can be helpful for reservoir engineering calculations, and steam management in geothermal fields. Currently, enthalpy of geothermal steam can be measured continuously at surface. The advantage of measuring enthalpy downhole is that it gives more direct information about the enthalpy of the reservoir fluids. The main challenges of measuring downhole are that the measurement device must be able to withstand harsh conditions, high temperatures and erosive fluids. At present, methods utilizing optical fiber are being investigated, thereby avoiding having to use downhole electronics.

6.2 ENTHALPY MEASUREMENTS

6.2.1 Enthalpy and Enthalpy Rate

Enthalpy is a property of a system that can be defined (per unit mass) as:

$$h = u + Pv \quad [\text{kJ/kg}] \quad \underline{\hspace{2cm}} \quad (6.1)$$

Here u is the internal energy of the system per unit mass, P is the pressure and v is the specific volume. Enthalpy is a thermodynamic property and can therefore be found from P-v-T relations given two of the parameters P , v and T . For flowing fluids it is in most cases easiest to evaluate P and T , however at saturation conditions the temperature and pressure become fixed with respect to each other. Hence the specific volume, v , must be determined to find the enthalpy. At saturation (boiling) conditions the fluid is partially evaporated so to give an estimate of the specific volume the vapor-liquid fraction needs to be determined. It will be defined as:

$$x = \frac{m_{\text{vapor}}}{m_{\text{total}}} \quad [-] \quad (6.2)$$

Here m_{vapor} and m_{total} are the mass of the vapor and the total fluid mixture respectively. Given this fraction and the saturation pressure or temperature, the specific volume can be found, or more directly, the enthalpy using the steam tables.

$$h_{@T_{\text{sat}}} = h_g + xh_{fg} \quad [\text{kJ/kg}] \quad (6.3)$$

Here h_g is the enthalpy of the saturated vapor and h_{fg} is the enthalpy of vaporization.

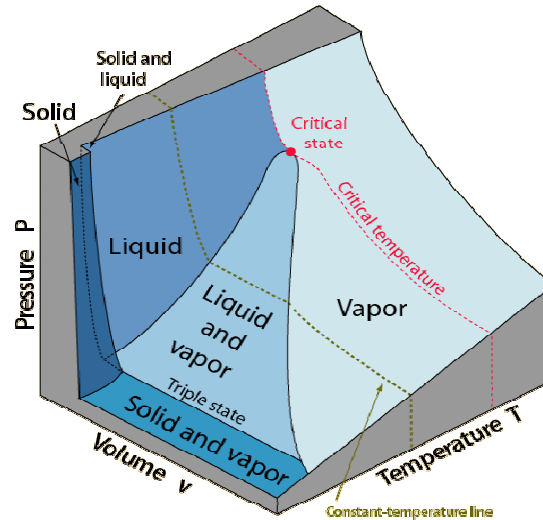


Figure 6.1: P - v - T relations for a substance. At saturation (vapor-liquid) conditions P and T become fixed with respect to each other. (<http://hyperphysics.phy-astr.gsu.edu>)

Looking at a flowing fluid it is often useful to know the rate of enthalpy (e.g. in geothermal energy utilization) through a fixed volume or cross section. To be able to determine this, the flow rate of the fluid must be known. If the fluid is flowing in two phases (is at saturation conditions) the flow rate of each phase must be known. In vertical flow the presence of buoyancy and frictional forces greatly complicates the relation between the velocities of the two phases. Some empirical relations have been suggested, e.g. by Hughmark and Pressburg (1961) at least for a certain range of diameters (0.4 to 2.34 inches). Obviously this sort of a relation would be very useful because the flow rate of only either phase would have to be measured.

In summary, to be able to determine the rate of enthalpy of a flowing fluid at saturation conditions one needs to measure the temperature (or pressure), the specific vapor-liquid volume fraction and both the flow rates of the vapor phase and the liquid phase (or of one of the phases, plus the total).

6.2.2 Existing measurement techniques

Existing techniques for measuring enthalpy in two-phase flow from geothermal wells are the tracer dilution method and resistivity measurements. The tracer dilution method is quite cumbersome and is typically performed only once a year. The resistivity measurement technique developed by Spielman (2003) gives continuous enthalpy values but it is designed for surface applications. Modifying this method to work downhole would be complicated because of the reaction of the electronics to the harsh downhole environment.

The use of optical fiber to measure downhole pressure and temperature has proven to work and is a good way to avoid problems with downhole electronics. The idea of expanding this technique to obtain a value of the enthalpy is one of the possibilities being considered in this project.

6.3 WHY MEASURE ENTHALPY?

6.3.1 Real-Time Enthalpy Measurement

Many geothermal plants are now working on development of real-time steam quality monitoring systems. These are useful because they provide a means to prevent excessive moisture from entering the turbine, thereby lowering its efficiency and causing for example erosive damage. The enthalpy rate from a geothermal well is one of the factors impacting the measurement of steam quality. Hence by continuously monitoring the enthalpy (as opposed to using a constant value updated once a year) improved steam quality control can be obtained.

6.3.2 Advantages of Downhole Measurement

What are the advantages of doing the measurements downhole? Firstly, during the evaluation stage of a project, it would be feasible to determine the reservoir enthalpy without having to conduct a long term flow test in order to heat up the entire wellbore, a process that can take several weeks. A second use would be the ability to measure the enthalpy at any given depth of the well. This could be used to verify results from with well flow simulations, thereby helping to improve reservoir modeling techniques. In relation to this it might be interesting to see if and where fractures carrying hot or cold water cross the well and how the enthalpy is affected by those entries. Thirdly, comparing the downhole enthalpy to the surface enthalpy could be useful in estimating the effects of wellbore heat losses if one wanted to make a more comprehensive model of the reservoir status.

6.4 PROPOSED METHODS AND PRESENT STATUS

6.4.1 Enthalpy from temperature deviations

A convenient way to solve the problem of finding the downhole enthalpy may be to use optical fiber. If a temperature difference between a vapor bubble and its surrounding liquid can be detected and the velocity can be determined from a characteristic signal from the bubble, then an estimate of the enthalpy can be inferred. As a result, the project would reduce to finding a calibration technique that would encompass the variety of flow conditions occurring in two-phase vertical pipe flow. In other words, the aim is not necessarily to find the liquid-volume fraction but rather to measure a signal that behaves generally in a way that is consistently relatable to the enthalpy.

At present, this is the solution being investigated. The initial step is to see if a temperature difference can be detected in air-water, two-phase flow (at room temperature) using high precision thermocouples (we are not using optical fiber yet, because data acquisition devices for optical fiber measurements are very expensive). Two of the main challenges are; obtaining a thermocouple that has an adequately fast response time to detect the bubble as it goes by; lowering the noise in the temperature measurement so that the minute temperature difference can actually be detected. This noise could probably be filtered out by post processing but an alternative measurement technique (e.g. optical measurement) to compare the signal to has not yet been implemented (but it is planned).

6.4.2 Resistivity or equivalent techniques

Using resistivity or some other means of sending a signal affected by vapor-liquid changes between two points is a method that is likely to work. This however would require building a new device specifically for this purpose and would probably lead to the much undesired downhole electronics. If looking at temperature deviations will not work this will be the next thing to try. An initial analysis of the problem follows.

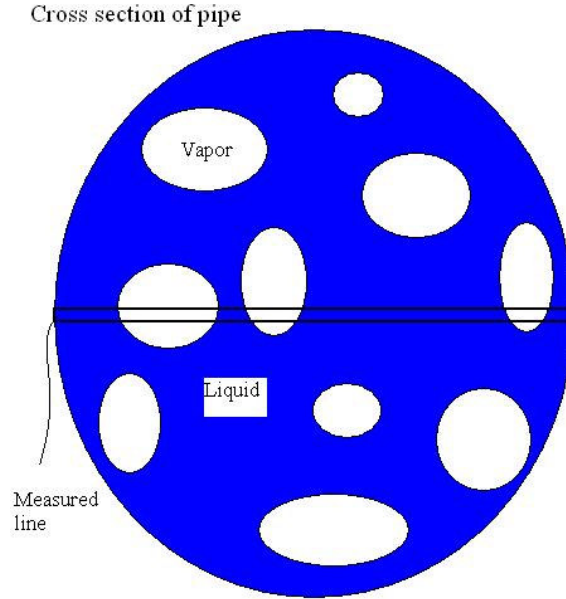


Figure 6.2: Cross section of pipe with vapor-liquid flow. A resistivity measurement (or equivalent) is being taken at multiple points across the “measured line”.

The goal is to find the enthalpy rate i.e. energy passing through the cross sectional area

$$A = A_f + \sum_i A_{gi} \quad [\text{m}^2] \quad (6.4)$$

(where A_f is the area occupied by liquid and A_{gi} is the area occupied by vapor bubble i) per time unit. The energy rate of the saturated vapor (h_g) and liquid (h_f) can be found from the steam tables and given the flow velocity (u) of each phase the flow rate can be found from

$$q_g = u_g \sum_i A_{gi} = u_g y A \quad [\text{m}^3/\text{s}] \quad (6.5)$$

$$q_f = u_f \left(A - \sum_i A_{gi} \right) = u_f (1 - y) A \quad [\text{m}^3/\text{s}] \quad (6.6)$$

Then the total enthalpy rate for each phase can be found as

$$\dot{H}_g = \frac{h_g q_g}{v_g} \quad [\text{J/s}] \quad (6.7)$$

$$\dot{H}_f = \frac{h_f q_f}{v_f} \quad [\text{J/s}] \quad (6.8)$$

Here the specific volumes v_g and v_f can be obtained from the steam tables, and the total enthalpy of the mixture is:

$$\dot{H} = \dot{H}_g + \dot{H}_f = \frac{h_g A y u_g}{v_g} + \frac{h_f A (1-y) u_f}{v_f} \quad [\text{J/s}] \quad (6.9)$$

So the average fraction of the cross section occupied by steam needs to be determined, i.e.

$$y = \frac{\sum_i A_{gi}}{A} \quad [-] \quad (6.10)$$

Suppose a measurement is taken at multiple points along a line across a cross section of a pipe (Figure 6.2). Assuming the bubbles will flow randomly through the cross section of the pipe the fraction of the line that is occupied by vapor, averaged over time, should give the fraction of steam going through the whole cross section (Figure 6.3).

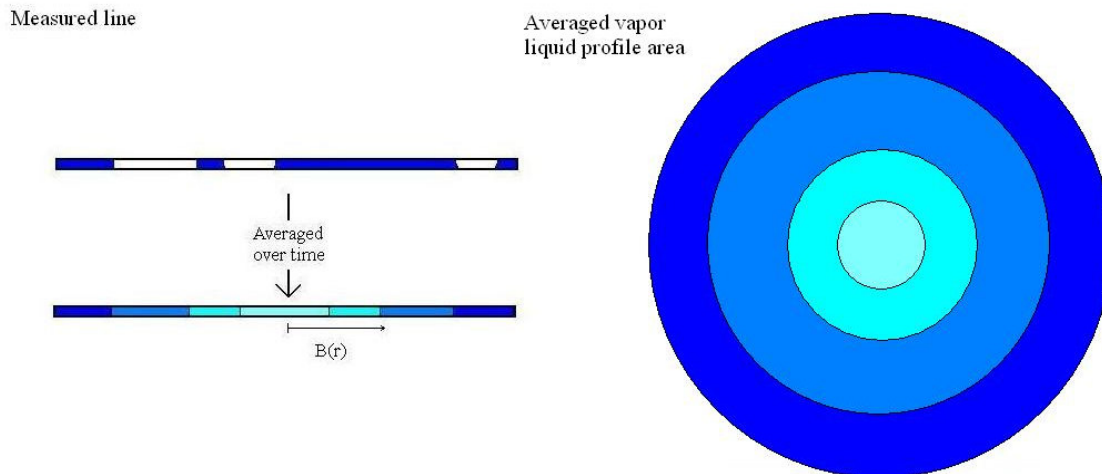


Figure 6.3: The measured lined averaged over time will likely form a symmetric distribution of vapor concentration. Lighter blue means more time on average occupied by vapor.

If $B(r)$ is defined as the time the measurement line is occupied by vapor at radius r divided by the total time the measurement is taken then as time goes by B will likely form a smooth symmetric distribution, e.g. something like the one depicted on the left part Figure 6.3. Integrating the distribution, $B(r)$, back over the cross sectional area gives the area occupied by steam on average, $A_{g,av}$ and dividing by the total area gives the quantity y as

$$y = \frac{A_{g,av}}{A} = \frac{\int_0^{D/2} 2\pi r B(r) dr}{\pi D^2 / 4} = \frac{8}{D^2} \int_0^{D/2} r B(r) dr \quad [-] \quad (6.11)$$

From this it seems that it would suffice to measure the resistivity along a single line across the pipe diameter. How the velocity of the vapor and liquid could be found has not been resolved.

6.5 CONCLUSION

Finding a way to measure downhole enthalpy is a challenging task. A number of methods have been proposed and more work needs to be put into testing what will actually work. At present a method using temperature deviations between vapor and liquid in two-phase flow is being investigated. Ultimately these measurements would be obtained from optical fiber sensors which have proven to work well in downhole data logging. Investigation of other methods is at an initiation stage.

7. REFERENCES

- Archie, G.E.: "The Electrical Resistivity Log as an Aid in Determining some Reservoir Characteristics," AIME Petroleum Tech. (1942), 1-8.
- Akhatov I., Lindau O., Topolnikov A., et al.: "Collapse and Rebound of a Laser-Induced Cavitation Bubble," *Physics of Fluids* (2001), Vol. **13**, p.2805-2819.
- Aziz, K. and Govier, G.W.: *The Flow of Complex Mixtures in Pipes*, Van Nostrand Reinold Company, 1972, pages 338-339.
- Babchin, A. J. and Yuan, J.-Y.: "On the Capillary Coupling Between Two Phases in a Droplet Train Model," *Transport in Porous Media* (1997), Vol. **26**, p.225-228.
- Boles, M.A. and Çengel, Y.A.: *Thermodynamics, An Engineering Approach*, McGraw-Hill Companies, Inc., 2002.
- Bretherton, F.P.: "The Motion of Long Bubbles in Tubes," *J. Fluid Mech.* (1961), Vol. **10**, p. 166-188.
- Brooks, R.H. and Corey, A.T.: "Hydraulic Properties of Porous Media," Colorado State University, Hydro paper No.5 (1964).
- Carey, V.P., *Liquid-Vapor Phase-Change Phenomena*, Hemisphere Publishing Corporation, New York, NY, February, 1992.
- Chen, C.-Y., Li, K., and Horne, R.N.: "Experimental Study of Phase Transformation Effects on Relative Permeabilities in Fractures," paper SPE 90233, presented in SPE 2004 Annual Technical Conference and Exhibition, Houston, TX, USA, September.26-29, 2004.
- Foulser, R. W. S., Goodyear, S. G. and Sims, R. J.: "New Concepts in Relative Permeabilities at High Capillary Numbers for Surfactant Flooding," *Transport in Porous Media* (1991), Vol. **6**, p. 223–240.
- Fujikawa, S., and Maerefat, M.: "A Study of the Molecular Mechanism of Vapor Condensation," *JSME International Journal* (Nov. 1990), Vol. **2**, No. 33, p. 634-641.
- Habana, M.D.: "Relative Permeability of Fractured Rock", MS report, Stanford University, Stanford, California, (2002).
- Horne, R.H., Satik, C., Mahiya, G., Li, K., Ambusso, W., Tovar, R., Wang, C., and Nassori, H.: "Steam-Water Relative Permeability," Proc. of the World Geothermal Congress 2000, Kyushu-Tohoku, Japan, May 28-June 10, 2000.
- Horne, R.N., Reyes, J.L.P., Li, K.: "Estimating Water Saturation at The Geysers Based on Historical Pressure and Temperature Production Data by Direct Measurement," Final Report to California Energy Commission, June 2003.
- Hughmark, G.A., and Pressburg, B.S.: "Holdup and pressure drop with gas-liquid flow in a vertical pipe," A.I.Ch.E. Journal, Vol. 7, p.677 (1961).

- Hunt, A.G., and Manga, M.: "Effects of Bubbles on the Hydraulic Conductivity of Porous Materials -- Theoretical Results," *Transport in Porous Media* (2003), Vol. **52**, p. 51-65.
- Kucherov, R.Y., and Rikenglaz, L.E.: "The Problem of Measuring the Condensation Coefficient," *Doklady Akad. Nauk. SSSR*, Vol. **133**, No.5, p. 1130-1131 (1960.)
- Kucherov, R.Y., and Rikenglaz, L.E, *Zh. Eksperim. i Teor. Fiz.* 37, 125 (1959) [English Transl.: *Sov. Phys.- JETP* 10, 88 (1960)].
- Li, K.: "Generalized Capillary Pressure and Relative Permeability Model Inferred from Fractal Characterization of Porous Media," SPE 89874, presented at the 2004 SPE Annual Technical Conference and Exhibition, Houston, Texas, U.S.A., 27 – 29 September 2004.
- Li, K. and Horne, R.N.: "Steam-Water Capillary Pressure," SPE 63224, presented at the 2000 SPE Annual Technical Conference and Exhibition, Dallas, TX, USA, October 1-4, 2000.
- Li, K. and Horne, R.N.: "Experimental Verification of Methods to Calculate Relative Permeability Using Capillary Pressure Data," SPE 76757, Proceedings of the 2002 SPE Western Region Meeting/AAPG Pacific Section Joint Meeting held in Anchorage, Alaska, May 20-22, 2002.
- Li, K., Nassori, H., and Horne, R.N.: "Experimental Study of Water Injection into Geothermal Reservoirs," presented at the GRC 2001 annual meeting, August 26-29, 2001, San Diego, USA; *GRC Trans.* V. **25**.
- Mahiya, G.: "Experimental Measurement of Steam-Water Relative Permeability," MS report, Stanford University, Stanford, California (1999).
- Molinari, M.: *High Fidelity Imaging in Electrical Impedance Tomography*, Ph.D. dissertation, University of Southampton, Southampton, United Kingdom (2003).
- O'Connor, P.A.: "Constant-Pressure Measurement of Steam-Water Relative Permeability," MS report, Stanford University, Stanford, California (2001).
- Partin, J.K., Davidson, J.R., Sponsler, E.N. and Mines, G.L.: "Deployment of an Optical Steam Quality Monitor in a Steam Turbine Inlet Line," presented at the Geothermal Resource Council 2004 annual meeting, August 29- September 1, 2004, Indian Wells, California, USA; *GRC Trans.* **28** (2003).
- Piquemal, J.: "Saturated Steam Relative Permeabilities of Unconsolidated Porous Media," *Transport in Porous Media* (1994), Vol. **17**, p. 105-120.
- Polydorides, N.: *Image Reconstruction Algorithms for Soft-Field Tomography*, Ph.D. dissertation, University of Manchester, Manchester, United Kingdom (2002).
- Purcell, W.R.: "Capillary Pressures-Their Measurement Using Mercury and the Calculation of Permeability", *Trans. AIME*, (1949), 186, 39.

- Ratulowski, J. and Chang, H.-C.: "Transport of Gas Bubbles in Capillaries," *Phys. Fluids A* (1989), Vol. **1**, p. 1642–1655.
- Sanchez, J.M and Schechter, R.S.: "A Comparison of the Two-Phase Flow of Steam/Water and Nitrogen/Water Through an Unconsolidated Permeable Medium," SPE 16967, paper presented at the 62nd SPE Annual Technical Conference and Exhibition, Dallas, Texas, USA, September 27-30, 1987.
- Sanyal, S.K.: The Effect of Temperature on Electrical Resistivity and Capillary Pressure Behavior of Porous Media, Ph.D. report, Stanford University, Stanford, Calif., 1972.
- Satik, C.: "A Measurement of Steam-Water Relative Permeability," Proceedings of 23rd Workshop on Geothermal Reservoir Engineering, Stanford University, Stanford, California (1998).
- Satik, C.: "A Study of Steam-Water Relative Permeability," paper SPE 46209 presented at the 1998 SPE Western Regional Meeting, Bakersfield, California, May. 10-13.
- Silver, R.S., and Simpson, H.C.: "The Condensation of Superheated Steam," Proc. of a conference held at the National Engineering Laboratory, Glasgow, Scotland, 1961.
- Spielman, P.: "Continuous Enthalpy Measurement of Two-Phase Flow from a Geothermal Well," presented at the Geothermal Resource Council 2003 annual meeting, October 12-15, 2003, Morelia, Mexico; *GRC Trans.* **27** (2003).
- Stark, J. and Manga, M.: "The Motion of Long Bubbles in a Network of Tubes," *Transport in Porous Media* (2000), Vol. **40**, p. 201-218.
- van Weereld, J.J.A., Player M.A., Collie, D.A.L, Watkins, A.P., Olsen, D.: "Flow Imaging in Core Samples by Electrical Impedance Tomography," paper SCA 2001-06, Society of Core Analysts.
- Verma, A.K.: *Effects of Phase Transformation of Steam-Water Two-Phase Relative-Permeability*, Ph.D. dissertation, University of California, Berkeley (1986).
- Wong, H., Radke, C. J. and Morris, S.: "The Motion of Long Bubbles in Polygonal Capillaries. 1. Thin Films," *J. Fluid Mech.* (1995a), Vol. **292**, p. 71–94.
- Wong, H., Radke, C. J. and Morris, S.: "The Motion of Long Bubbles in Polygonal Capillaries. 2. Drag, Fluid Pressure and Fluid flow," *J. Fluid Mech.* (1995b), Vol. **292**, p. 95–110.